Remote Sensing of Environment 260 (2021) 112468

Contents lists available at ScienceDirect

Remote Sensing of Environment

journal homepage: www.elsevier.com/locate/rse

CNN-based burned area mapping using radar and optical data

Miguel A. Belenguer-Plomer [a,b,*], Mihai A. Tanase [a], Emilio Chuvieco [a], Francesca Bovolo [b]

[a] Environmental Remote Sensing Research Group, Dep. of Geology, Geography and Environment, Universidad de Alcalá, Alcalá de Henares 28801, Spain
[b] Center for Information and Communication Technology, Fondazione Bruno Kessler, Trento 38122, Italy

ARTICLE INFO

Editor: Marie Weiss

Keywords:
Burned area mapping
Convolutional neural networks
Deep learning
SAR
Sentinel-1
Sentinel-2
Wildland fires

ABSTRACT

In this paper, we present an in-depth analysis of the use of convolutional neural networks (CNN), a deep learning method widely applied in remote sensing-based studies in recent years, for burned area (BA) mapping combining radar and optical datasets acquired by Sentinel-1 and Sentinel-2 on-board sensors, respectively. Combining active and passive datasets into a seamless wall-to-wall cloud cover independent mapping algorithm significantly improves existing methods based on either sensor type. Five areas were used to determine the optimum model settings and sensors integration, whereas five additional ones were utilised to validate the results. The optimum CNN dimension and data normalisation were conditioned by the observed land cover class and data type (i.e., optical or radar). Increasing network complexity (i.e., number of hidden layers) only resulted in rising computing time without any accuracy enhancement when mapping BA. The use of an optimally defined CNN within a joint active/passive data combination allowed for (i) BA mapping with similar or slightly higher accuracy to those achieved in previous approaches based on Sentinel-1 (Dice coefficient, DC of 0.57) or Sentinel-2 (DC 0.7) only and (ii) wall-to-wall mapping by eliminating information gaps due to cloud cover, typically observed for optical-based algorithms.

1. Introduction

Fire is one of the natural disturbance processes that generates significant social and economic consequences (Bowman et al., 2020; Chuvieco et al., 2010) and modifies the terrestrial ecosystems by reducing biodiversity, changing water supply and liberating vegetated-sequestered carbon (Hansen et al., 2013; Aponte et al., 2016; Pausas and Paula, 2012; Lavorel et al., 2007). At global scale, emissions of aerosols and greenhouse gases (GHGs) from fires may modify the Earth's biochemical cycles and the radiative energy balance (Van Der Werf et al., 2017; Bowman et al., 2009; Jin and Roy, 2005). Fire-induced carbon emissions have been estimated to be 2.2 PgC per year over the period 1997–2016 (Van Der Werf et al., 2017), which translates into 20–30% of global emissions from burning fossils fuels, triggering the current global warming (Kloster et al., 2012; Flannigan et al., 2009). Besides, it is observed a direct relationship between the rising of Earth's temperature and the severity of fires (Hoffmann et al., 2002; Knorr et al., 2016). Given the global warming current context, such a relationship may reinforce the fire role progressively on climate change (Turco et al., 2019; Williams and Abatzoglou, 2016; Flannigan et al., 2006; Langenfelds et al., 2002). However, fires may also result in opposite effects by enabling global cooling processes as a result of increased aerosols in the atmosphere, which induce negative radiative forcing (Ward et al., 2012). Such effects suggest a limited understanding of fire impact on global climate (Krawchuk et al., 2009; Liu et al., 2019).

Due to its undeniable climatic and environmental importance, fire is considered by the Global Climate Observing System (GCOS) as an Essential Climatic Variable (ECV) (i.e., a physical, biological, chemical, or a group of connected variables capable of altering the climate system (Bojinski et al., 2014)). The European Space Agency (ESA), through the Climate Change Initiative (CCI) programme, is generating remote sensing-based ECVs to improve climate modelling (Plummer et al., 2017; Hollmann et al., 2013). Fire has been included in the CCI programme since 2010 (Fire_cci project). Improving current BA products by developing new algorithms based on state-of-the-art Earth observation datasets as well as generating a long-term time series of global BA have been the main goals of the Fire_cci project (Chuvieco et al., 2018). One driving factor behind the project was the need for more accurate BA products that reduce current uncertainties when studying the fire-induced climate impacts (Mouillot et al., 2014; Poulter et al., 2015).

* Corresponding author at: Environmental Remote Sensing Research Group, Dep. of Geology, Geography and Environment, Universidad de Alcalá, Alcalá de Henares 28801, Spain.
E-mail address: miguel.belenguer@uah.es (M.A. Belenguer-Plomer).

https://doi.org/10.1016/j.rse.2021.112468
Received 14 May 2020; Received in revised form 16 April 2021; Accepted 19 April 2021
Available online 24 April 2021

In particular, emissions from small-sized fires were of particular concern (Van Der Werf et al., 2017; Ramo et al., 2021).

Many BA global products have been released over the past decade, mostly based on optical imagery acquired by the Moderate Resolution Imaging Spectroradiometer (MODIS), such as the MCD45 (Roy et al., 2008), MCD64 (Giglio et al., 2009, 2018), Fire_cci v5.0 (Chuvieco et al., 2018) and Fire_cci v5.1 (Lizundia-Loiola et al., 2020). However, such products have limitations as small-sized fires are difficult to detect due to the coarse pixel spacing (>250 m). Such limitations generate uncertainty about the extent of the global burned area (Chuvieco et al., 2019). In order to reduce BA mapping uncertainty, imagery acquired by medium spatial resolution optical sensors such as Landsat-8 and Sentinel-2 are increasingly used to map BA at regional and global scales. Indeed, a recent study over sub-Sahara Africa based on Sentinel-2 images for 2016 quantified an increase of 80% over existing global BA products (MCD64A1 product Version 6) for the same region and year (Roteta et al., 2019). In addition to problems observed when detecting small-sized fires, global BA products are also affected by cloud cover, which limits detection of burned pixels, particularly in Tropical regions where fire activity occurs over short time spans and the continuous cloud cover prevents BA mapping from optical sensors. In order to circumvent such limitations, active sensors (e.g., synthetic aperture radar – SAR) have been used as an alternative to optical imagery for mapping BA (Bourgeau-Chavez et al., 2002; French et al., 1999). The launch of ESA's Sentinel-1 A and B in October 2014 and December 2015, respectively, have greatly improved the availability of SAR images, by operationally acquiring (i) dual-polarisation C-band imagery (i.e., vertical–vertical, VV, and vertical–horizontal, VH polarisations), while (ii) providing precise orbital information, (iii) allowing for viewing geometries more suitable for vegetation monitoring through increased incidence angle, and (iv) improving spatial and temporal resolution, as revisit period of Sentinel-1 mission is three days when combining ascending and descending passes from Sentinel-1 A and B. Such advances, coupled with a free data access policy, have allowed for the development of SAR-based BA mapping algorithms (Belenguer-Plomer et al., 2019c). Indeed, a first large-scale BA product based on Sentinel-1 datasets was released recently for the Amazon basin for the year 2017 (https://www.esa-fire-cci.org/, last accessed March 15th, 2020).

Availability of near-concurrent active (Sentinel-1) and passive (Sentinel-2) datasets allows taking advantage of similar spatial and temporal resolutions of radar and optical information. Nevertheless, few studies have considered combining such sensors when mapping BA. In addition, there is little consensus regarding the benefits of such data combination. Some studies noted that active-passive data might reduce limitations associated with each data-source (Verhegghen et al., 2016). On the contrary, other studies suggest limited to nil benefits (Brown et al., 2018). The potential of radar-optical based approaches depends on several limiting factors depending on the sensor type. Optical sensors are severely restricted by cloud cover or strong variations in solar illumination (Bourgeau-Chavez et al., 2002; French et al., 1999). Limitations to using SAR for fire mapping include sensitivity of SAR backscatter to variations in soil moisture and steep topography (Belenguer-Plomer et al., 2018, 2019a). Besides, BA detection and mapping accuracy from both types of sensors is affected by the land cover class (Tanase et al., 2020). Previous studies which investigated the potential of combining SAR-optical (SAR—O) for BA mapping did it only over relatively small study areas or single biomes, which reduced results validity (Verhegghen et al., 2016; Brown et al., 2018; Stroppiana et al., 2015). Furthermore, the strengths and weaknesses of combining active and passive datasets within a single BA classification algorithm as opposed to a single sensor-based detection and post-detection fusion have only been superficially analysed.

Deep learning methods have been widely applied, in recent years, in many remote sensing-based studies (Zhu et al., 2017). Among them, the convolutional neural networks (CNN) are being extensively used for classifying satellite images (Ma et al., 2019), although few studies address BA detection and mapping (Ban et al., 2020; Pinto et al., 2020). The present research has been motivated by the limited literature on CNN applied to BA mapping, and the need for a more profound understanding of its strengths and limitations over existing classification approaches, and particularly, the impact of different configurations on BA detection accuracy, as well as the relevance of the burned land cover, level of fire severity and water content variations of soil and vegetation when using SAR data on detection performance (Belenguer-Plomer et al., 2019c). This paper analyses the CNN potential for BA mapping when SAR and optical data are combined, considering a wide range of burning conditions. Data from Sentinel-1, Sentinel-2 and their combination have been used to test different CNN configurations for detecting burned pixels. The analysis was carried out over distinct ecosystems and biomes with significant fire activity. The specific objectives of the study were to (i) determine the optimum CNN parameters (i.e., image dimensionality for feature extraction, data normalisation, and the number of hidden layers) for each input dataset (i.e., radar, optical and SAR—O) and land cover class, and (ii) to find the optimal active-passive combination approach for BA mapping. The optimal configuration was validated over independent study areas.

2. Study areas and datasets

Ten Military Grid Reference System (MGRS) tiles, distributed over most of the biomes frequently affected by fires, were used as study areas. These tiles covered a broad range of terrestrial ecoregions, land cover classes, fire intensity (radiative power) as well as soil moisture and precipitation patterns over the considered fire periods (Table 1). Notice that no site was selected within the boreal region since there were found too specific and not generalisable effects, such as the fire-induced permafrost layer melting which increases the soil moisture. (Bourgeau-Chavez et al., 2002; Kasischke et al., 1994). Thus, additional research focused on this biome must be carried out in future attempts. Five of the tiles (training tiles) were used to calibrate the algorithm, which included finding the optimum mapping configuration (i.e., CNN parameters and sensor combination). The remaining tiles (test tiles) were reserved for validating the results over independent sites, as well as checking the algorithm generalisation capability (Fig. 1).

Ground range detected (GRD) C-band backscatter coefficient temporal series acquired by the Sentinel-1 A and B satellites using the interferometric wide (IW) swath mode were the source of radar information. Temporal series acquired by the MultiSpectral Instrument (MSI) on-board the Sentinel-2 A and B satellites were the source of optical information. Sentinel-1 and Sentinel-2 data were downloaded from Copernicus Open Access Hub. As ancillary data, the enhanced Shuttle Radar Topography Mission (STRM) Digital Elevation Model (DEM) at 30 m pixel spacing was considered when pre-processing both SAR and optical datasets (see Section 3.1). Ancillary datasets such as land cover information as well as thermal anomalies due to active fires (i.e., hotspots) were also used within the BA mapping algorithm. The land cover information was extracted from the ESA's land cover CCI product for the year 2015 Land_Cover_cci, which uses the Land Cover Classification System (LCC) (Di Gregorio, 2005). The LCC legend was simplified to six landscapes (i.e., shrublands, grasslands, forests, crops, non-burnable and others, including the later transitional woodland-shrub and sclerophyllous vegetation) as in our previous research study to simplify the BA mapping procedure (Belenguer-Plomer et al., 2019c). Hotspots from VIIRS (Visible Infrared Imaging Radiometer Suite) (Schroeder et al., 2014) and MODIS (Giglio et al., 2016) sensors at 375 m and 1 km of spatial resolution, respectively, were downloaded from NASA's Fire Information for Resource Management System (FIRMS).

Reference fire perimeters were used to validate the BA products. The reference perimeters were derived from independent sensors (i.e., Landsat imagery) to avoid auto-correlation (Tanase et al., 2020). Landsat-8 BOA (bottom of atmosphere) reflectance images with cloud cover below 70% were downloaded from the United States geological

Table 1
Terrestrial ecoregions (Olson et al., 2001), predominant land cover classes (from CCI[1] land cover, 2015), mean fire radiative power (FRP, derived from VIIRS[2] and MODIS[3] thermal anomalies products), pre- and post-fire soil moisture (SM, from SMAP[4] product), and accumulated precipitations (from CHRIPS[5] product) for each MGRS tile. Notice that ± is referring to the standard deviation.

MGRS	Terrestrial ecoregion	Predominant land covers	FRP (MW)	SM pre-fire (m^3/m^3)	SM pos-fire (m^3/m^3)	Rainfall (mm)
10UEC	Tcf	F (76.7%), S (7.9%) and G (7.2%)	17.5±24.6	0.11±0.03	0.11±0.03	2.4
10SEH	Mfws	G (24.59%), C (24.22%) and F (19.23%)	10.0± 4.51	0.1±0.03	0.17±0.03	4.79
20LQQ	TSTmbf	F (93.8%), C (3.7%) and S (2.1%)	13.86±16.13	0.33±0.06	0.24±0.05	3.61
20LQP	TSTmbf	F (93.1%), C (5.7%) and S (1.01%)	13.78±14.5	0.1±0.05	0.13±0.03	1.77
29TNG	Tbf	S (36.1%), F (26.5%) and C (10.6%)	24.9±33.06	0.09±0.02	0.18±0.02	4.73
29TNE	Mfws	S (45%), F (28.3%) and C (12.7%)	24.9±33.06	0.07±0.03	0.07±0.03	0.24
33NTG	TSTgss	F (89.4%), S (10.1%) and O (0.06%)	9.03±7.37	0.23±0.04	0.09±0.03	91.2
36NXP	TSTgss	S (52.7%), F (41.3%) and C (4.7%)	14.24±14.68	0.13±0.06	0.12±0.05	17.64
50JML	Mfws	G (70.7%), S (12.9%) and F (9.7%)	13.03±13.69	0.11±0.02	0.07±0.01	146.63
52LCH	TSTgss	S (72.5%), O (25.7%) and G (0.4%)	8.98±9.12	0.2±0.04	0.18±0.03	24.25

Terrestrial ecoregion: Tcf - Temperate Coniferous Forests; Mfws - Mediterranean Forests, woodlands and scrubs; TSTmbf - Tropical and subtropical moist broadleaf forests; Tbf - Temperate broadleaf and mixed forests; TSTgss - Tropical and subtropical grasslands, savannas and shrublands.
Land covers: F - Forests; S - Shrubs; G - Grasslands; C - Crops; O - Others.
[1]CCI - Climate Change Initiative; [2] VIIRS - Visible Infrared Imaging Radiometer Suite; [3]MODIS - Moderate Resolution Imaging Spectroradiometer; [4]SMAP - Soil Moisture Active Passive; [5] CHIRPS - Climate Hazards Group InfraRed Precipitation with Station data.

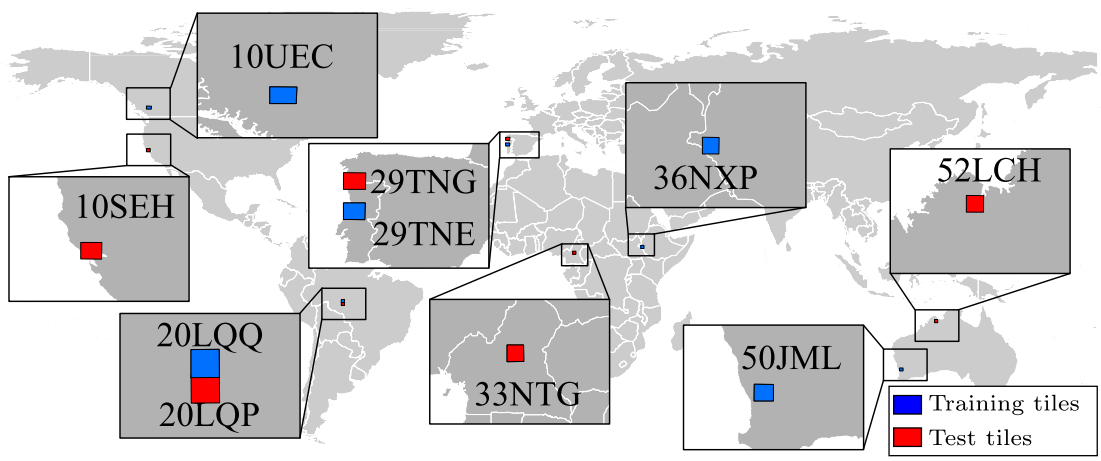

Fig. 1. Location of the military grid reference system tiles used for training and test.

survey repository (USGS) for each tile. The extraction of the reference fire perimeters is explained in detail in Section 3.4

3. Methods

3.1. Sentinel-1 pre-processing

Sentinel-1 GRD images were processed using the Orfeo ToolBox (OTB), an open-source software developed by the Centre National D'Etudes Spatiales (CNES), France (Inglada and Christophe, 2009). The processing chain has been utilised in previous studies (Belenguer-Plomer et al., 2019c,b; Ottinger et al., 2017; Bouvet et al., 2018) and when generating the FireCCIS1SA10 product, the first large-scale BA product from Sentinel-1 data for the Amazon basin. Sentinel-1 data processing may be divided into three steps: data-preparation, geocoding, and multi-temporal filtering (Fig. 2). Sentinel-1 data were calibrated radiometrically to gamma nought (γ^0) via a lookup table obtained from the product metadata. The calibrated imagery was orthorectified using topographical information from the SRTM DEM. Since ESA often provides Sentinel-1 images of the same relative orbit within distinct slices, images from the same orbit were mosaicked and then spatially trimmed to the coordinates of the MGRS tile. Lastly, the processed images of each orbit were temporally filtered (Quegan et al., 2000). All images were processed to the Sentinel-1 nominal resolution (20 m) and subsequently aggregated to 40 m to reduce speckle (Tanase and Belenguer-Plomer, 2018; Belenguer-Plomer et al., 2020).

BA mapping is an iterative process in which the fire-detection interval is delimited by the temporal gap between two consecutive data

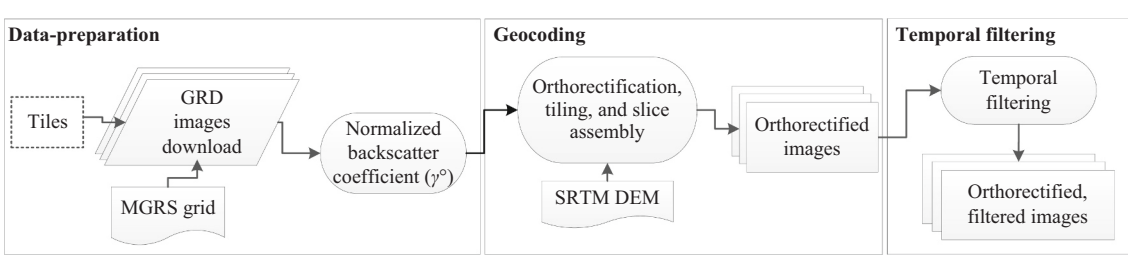

Fig. 2. Data chain pre-processing of SAR images with Orfeo ToolBox (Belenguer-Plomer et al., 2019c).

acquisitions. For each fire-detection interval (t_0), determined by two Sentinel-1 consecutive acquisition dates (t_{-1} and t_{+1}), the two most recent images acquired before t_0 (i.e., pre-fire) and all images acquired up to 180 days after t_0 (post-fire) were used as input for the CNN BA mapping algorithm. Both available polarisations (i.e., VV and VH) and their ratio (i.e., VH/VV) were considered for each SAR image sensing date. Notice that the log-ratio used in some SAR-based change detection studies was not included since it had lower relevance than simple SAR ratios when monitoring fire effects (Belenguer-Plomer et al., 2019a). The 180 days post-fire interval accounted for fire-induced temporal variation of the backscattering process that may occur at some point after a fire event due to temporal decorrelation Belenguer-Plomer et al. (2019b).

3.2. Sentinel-2 pre-processing

The ESA's atmospheric correction algorithm, sen2cor (v.2.4.0), was used to derive Sentinel-2 surface reflectance images by correcting not only atmospheric but also topographic effects. The bi-cubic interpolation was subsequently used to resample the 20 m Sentinel-2 images to the pre-processed Sentinel-1 output pixel spacing of 40 m. Temporal composites of Sentinel-2 images were generated to reduce the number of cloud-affected pixels using images acquired by both satellites for the selected bands (i.e., B02, B03, B04, B05, B06, B07, B8a, B11 and B12). Given a fire-detection interval (t_0), as determined by two consecutive acquisition dates of Sentinel-2 A and B (t_{-1} and t_{+1}), the sen2cor-based Scene Classification (SCL) was considered when generating the temporal composites for t_{-1} and t_{+1}. Pixels affected by clouds or shadows were gap-filled using data from Sentinel-2 imagery acquired at the closest date before t_{-1} and past t_{+1}, up to 30 days (Melchiorre and Boschetti, 2018) (Fig. 3).

Along with the surface reflectance for each of the two temporal composites (pre- and post-fire), the following indices were computed and fed into the CNN: (i) the Normalized Burn Ratio (García and Caselles, 1991) (NBR, Eq. (1)), (ii) the Normalized Difference Water Index (Gao, 1996) (NDWI, Eq. (3)), (iii) the Normalized Difference Vegetation Index (Rouse Jr et al., 1974; Tucker, 1979) (NDVI, Eq. (2)) and the (iv) Mid InfraRed Burn Index (Trigg and Flasse, 2001) (MIRBI, Eq. (4)). These indices are part of the state-of-the-art of BA mapping from optical datasets (Roteta et al., 2019; Loboda et al., 2007; Fraser et al., 2000).

$$NBR = (NIR\text{-}SWIR_2)/(NIR + SWIR_2) \quad (1)$$

$$NDVI = (NIR\text{-}Red)/(NIR + Red) \quad (2)$$

$$NDWI = (NIR\text{-}SWIR_1)/(NIR + SWIR_1) \quad (3)$$

$$MIRBI = 10 \times SWIR_2 - 9.8 \times SWIR_1 + 2 \quad (4)$$

where Red, NIR, SWIR1 and SWIR2 are the surface reflectances of bands 4 (650–680 nm), 8a (785–899 nm), 11 (1565–1655 nm) and 12 (2100–2280 nm) of MSI on-board Sentinel-2 satellites, respectively.

3.3. SAR-optical data integration

As Sentinel-1 and Sentinel-2 acquisition dates may not coincide when capturing images over the same geographical area, the Sentinel-1 acquisition dates defined each fire-detection interval (t_0) when jointly using SAR and optical data because of their complete spatial coverage (i.e., no missing pixels due to cloud cover). Then, Sentinel-2 images were matched to the Sentinel-1 dates for each detection period as follows when there was not any temporally coincident image: for the pre-fire date, the closest Sentinel-2 image acquired before was selected as t_{-1} date, whereas for the post-fire date, the closest image acquired after was selected as t_{+1} date. Once the Sentinel-2 images were matched with the Sentinel-1 detection interval, cloud-related gaps were filled through carrying out the temporal composite process (see Section 3.2). Subsequently, the Sentinel-1 radar-derived images (i.e., VV, VH and VH/VV ratio) acquired on t_{-1} and t_{+1}, as well as the Sentinel-2 temporal composites (i.e., spectral bands and spectral-indices) were stacked and fed into the classification algorithm. Similar data combination approaches based on Sentinel-1 and Sentinel-2 had been previously used for vegetation monitoring (Sharma et al., 2018; Tavares et al., 2019), also employing CNN (Scarpa et al., 2018).

3.4. Reference burned perimeters and validation

The reference fire perimeters were extracted from Landsat-8 surface reflectance. The extraction was based on the validation framework previously established for BA products (Padilla et al., 2014, 2015, 2017; Fernandez-Carrillo et al., 2018; Franquesa et al., 2020). A random forests classifier was trained using samples of burned, unburned and no

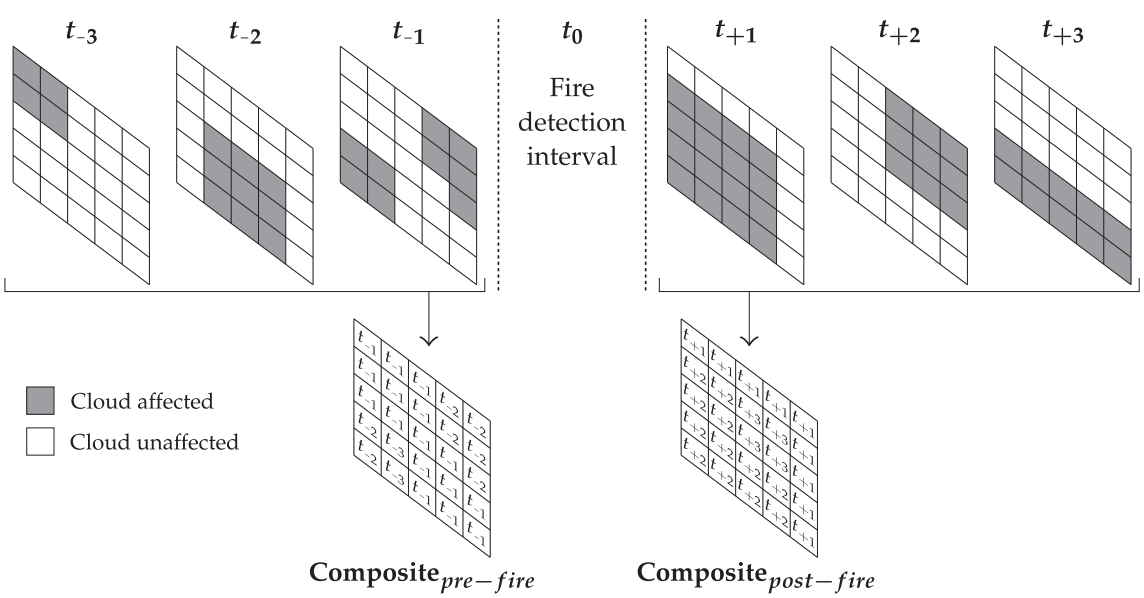

Fig. 3. Graphical representation of temporal composite formation. The fire-detection interval (t_0) is defined by the time span of two consecutive Sentinel-2 images, being dependent on the revisit period.

data pixels (i.e., clouds). These samples were selected through manual digitisation of polygons over a false colour composite (RGB: $SWIR_2$, NIR, R) which provided an experienced user with a clear visual distinction between burned, unburned and no data pixels. Input data for the random forests classifier were (i) the band 5 (NIR; 0.85–0.88 μm) and band 7 ($SWIR_2$; 2.11–2.29 μm) of post-fire date, (ii) the NBR of post-fire (Eq. (1)) and (iii) the temporal difference between pre- and post-fire of NBR values (dNBR) from Landsat-8 images. Model-training and scene classification was carried out iteratively, by including new training data in each iteration and re-running the classifier until the reference fire perimeters were considered accurate at close-up visual inspection.

Confusion matrices were used to validate the CNN-based BA maps (Table 2). The Dice coefficient (Eq. (5)) and the omission (Eq. (6)) and commission errors (Eq. (7)), which are widely used metrics when validating BA products, were computed from the matrix to assess the quality of the maps (Padilla et al., 2015).

$$\mathrm{DC} = 2P_{11}/(P_{1+} + P_{+1}) \tag{5}$$

$$\mathrm{OE} = P_{21}/P_{+1} \tag{6}$$

$$\mathrm{CE} = P_{12}/P_{1+} \tag{7}$$

3.5. Burned area mapping experimental setup

The BA mapping algorithm identifies changes in C-band backscatter and surface reflectance associated with burning events. BA mapping was carried out using (i) Sentinel-1 derived incoherent SAR-based metrics (see Section 3.1), (ii) Sentinel-2 surface optical reflectance (see Section 3.2) and (iii) combining SAR and optical selected datasets (see Section 3.3). Thus, up to three BA maps derived from different input datasets were generated for each detection period. Hotspots and land cover information were used for algorithm training purposes (see Section 3.5.2).

3.5.1. Convolutional neural networks (CNN) background

Deep learning methods are increasingly applied to remote sensing problems (Zhu et al., 2017) with CNN being widely used in land cover classification, the retrieval of bio-geophysical variables (Ma et al., 2019) or BA detection and classification (Ban et al., 2020; Pinto et al., 2020). CNNs are structured by stages of convolution and pooling, followed by at least one fully connected layer (LeCun et al., 2015; Zhu et al., 2017). Each convolutional layer carries out a spatial-spectral feature extraction (Zhong et al., 2019), generating a set of filtered data where patterns such as edges are emphasised (Strigl et al., 2010). From the convoluted filtered data, each neuron takes a vector and applies an activation function of a weighted linear summation (Eq. (8)) (Maggiori et al., 2016).

$$a = f(\mathbf{wx} + b) \tag{8}$$

where a is the neuron output, $\mathbf{w}$ is the weight given to the vector $\mathbf{x}$, b is the bias value, and f is the activation function which introduces non-linearity into the network and permits learning complex features from data (Agostinelli et al., 2014; Saha et al., 2019). The most common activation function in remote sensing applications is the rectified linear unit (ReLU) (Nair and Hinton, 2010), which activates values greater than zero, while it converts the remaining to zero (Eq. (10)).

Table 2
Confusion matrix scheme.

	Refererence data		
Detection	Burned	Unburned	Row total
Burned	P_{11}	P_{12}	P_{1+}
Unburned	P_{21}	P_{22}	P_{2+}
Col. total	P_{+1}	P_{+2}	N

$$f(x) = \begin{cases} x, & x \geq 0 \\ 0, & x < 0 \end{cases} \tag{9}$$

A loss function is used to quantify the errors when classifying a training vector data, comparing the CNN-based prediction with the label of such vector (Maggiori et al., 2016). The weights and biases of each neuron are adjusted using the backpropagation criterion during the network training, carrying out multiple iterations forward and backward (Anantrasirichai et al., 2019) to minimise the errors via gradient descent (Schmidhuber, 2015). The activated data is sub-sampled to reduce the tensor size, which increases the receptor field to the next convolutional layer of the network (Kellenberger et al., 2018; Strigl et al., 2010). The last layer of the network performs the classification instead of the feature extraction. Thus, a fully connected neural network is used. Usually, such a fully connected network is followed by a softmax layer, which models the input data to the probability of belonging to each considered class (Hu et al., 2015; Anantrasirichai et al., 2019; Zhang et al., 2018).

3.5.2. Selection of training data

CNN is a supervised learning method, and as such, it needs sample data (i.e., burned and unburned pixels) for training purposes. In this study, the training data extraction relied on hotspots and land cover information at each MGRS tile (100×100 km). Hence, a specific CNN model was built and trained for each fire-detection interval (t_0) and land cover class at each tile, which limited the large variations in climate regimes, vegetation classes or phenological cycles. The use of hotspots, well established for BA mapping (Belenguer-Plomer et al., 2019c; Roteta et al., 2019), was essential, especially when using the radar-derived metrics to differentiate changes due to fires (Huang and Siegert, 2006). In addition, processing pixels according to their land cover class allowed improving the patterns characterisation, which resulted in more accurate separation of burned and unburned areas when considering SAR, optical and both datasets (Belenguer-Plomer et al., 2018; Tanase et al., 2020). Therefore, CNNs training and the subsequent mapping process were carried out class-by-class, with the number of CNN models built depending on the land cover classes present in each study area. For a land cover class k, the training pixels of the burned category were selected within a spatial buffer determined as the double of the thermal sensor spatial resolution (Langner et al., 2007; Sitanggang et al., 2013). The unburned training pixels were those outside the hotspot buffer areas as well as from not burnable (e.g., water) land cover classes according to CCI land cover map reference.

3.5.3. Assessment of optimum CNN configuration for BA mapping

The architecture of the CNNs was based on AlexNet (Krizhevsky et al., 2012), and integrate hidden convolutional layers, the ReLU activation function, max-pooling, fully-connected layers, dropout and softmax classification. According to Bashiri and Geranmayeh (2011), the parameters of a CNN model, such as the number of layers, neurons and filters, have to be adjusted ad hoc for each dataset. Hence, up to eight different CNN-combinations by each input dataset were analysed to determine the optimal network for BA detection and mapping (Table 3).

Table 3
The eight configurations assessed for each input dataset (S – simple, C – complex).

CNN model	Convolution dimension	Data normalisation
S	1D	z-score
S	1D	[0, 1]
S	2D	z-score
S	2D	[0, 1]
C	1D	z-score
C	1D	[0, 1]
C	2D	z-score
C	2D	[0, 1]

Four architectures were analysed after combining two CNN-groups that differed in terms of (i) the number of hidden layers and filters, and (ii) the image domain where the convolutional feature extraction was executed (i.e., spatial or spectral). The first group included two CNN models with a different number of hidden layers and filters. The first model used two hidden layers with 32 and 64 filters, respectively, whereas the second model had a third additional hidden layer where 128 filters were applied. Hereafter the models with two and three hidden layers are referred to as the simple (S) and the complex (C), respectively. The second group involved two convolution-based filters for feature extraction. Given any pixel located at row i and column j of the input image $\mathbf{X}$, the first filter implied a pixel-wise convolution over the spectral domain (1D). It was considered a three-pixels size kernel to extract features from the spectral information of the previously stacked optical images and radar channels (see Section 3.1 to Section 3.3). The second filter considered a 3×3 kernel around the centre pixel (spatial domain, 2D) to extract the features used for BA detection (Kussul et al., 2017; Xu et al., 2017; Zhang et al., 2019) (Fig. 4).

Two normalisation methods were tested separately with each image band being normalised (i) in the interval [0, 1] (Benedetti et al., 2018) (Eq. 10) and (ii) applying the z-score normalisation (Zhong et al., 2017) (Eq. 11).

$$interval\ \ [0,1](x) = \frac{x}{max(b)} \tag{10}$$

$$z-score(x) = \frac{x-\mu(b)}{\sigma(b)} \tag{11}$$

where x is a given pixel of a band b of the image, and μ and σ are the mean and standard deviation, respectively. Table 3 shows the eight configurations for BA mapping performance assessment.

4. Results

4.1. Optimum CNN configuration

Depending on the MGRS tile, the optimum CNN configuration varied (Fig. 5). When Sentinel-1 (S-1) data were fed into the CNN, accuracy metrics dispersion (i.e., between tiles) at any CNN configuration was higher when compared to feeding Sentinel-2 (S-2) data or both Sentinel-1 and Sentinel-2 data (S-1 + S-2). The inter-tiles accuracy dispersion of the radar-fed CNN was lower when carrying out the convolution-based feature extraction through the spatial domain of the image (2D), which decreased omission errors (36NXP, 20LQQ and 50JML) despite a slight increase in commission errors for some tiles (10UEC and 29TNE). Similar results were achieved when feeding the CNN model using Sentinel-2 data only. Contrarily, when feeding both types of data (i.e., S-1 + S-2) into the CNN, the convolution dimension (i.e., 1D or 2D) did not influence the accuracy. In addition, the time required when training 2D models was lower compared to 1D, particularly when considering complex (C) networks, regardless of the data normalisation type. The use of more complex (C) CNN models, instead of using the simplest ones (S), did not increase the accuracy without regard to the type of data fed into the network. Similarly, training times were not influenced by the data normalisation method (z-score vs [0, 1]). However, a marginal enhancement of mapping accuracy was observed when using the z-score normalisation for the Sentinel-1 fed CNN, particularly in tile 50JML (i.e., Australian grasslands), where OE was reduced significantly (for 2D CNN). Conversely, when feeding Sentinel-2 or Sentinel-1 and Sentinel-2 data, the [0, 1] normalisation provided slightly more accurate BA detection rates.

By land cover classes, the lowest BA mapping accuracy was observed over Grasslands, particularly when using Sentinel-1 data due to high OE (Fig. 6). However, combining 2D convolution with z-score normalisation resulted in improved DC (by 59%) from 1D convolution-based approaches with z-score (DC 0.35±0.24 vs 0.22±0.2, mean ± the standard deviation). The same configuration (2D and z-score) also improved the accuracy over Crops, especially when compared to 1D with [0, 1] data normalisation (DC 0.37±0.14 vs 0.30±0.25), although to a lesser extent, while over Forests the improvement was marginal. Accuracy metrics were stable for Shrubs over all the configurations tested, although the 2D and z-score configuration provided less overall dispersion among the analysed tiles. In the Others class, the highest mapping accuracy based on Sentinel-1 data was achieved using the convolution in the spectral domain (1D).

Although Sentinel-2 fed CNN achieved higher accuracy when compared to Sentinel-1 fed one, such an improvement was conditioned by land cover classes and configurations. When using optical data, the spectral-based feature extraction (1D) was the most appropriate except for Crops, where the spatial-based (2D) improved the results. Besides, marginal differences in BA accuracy were found between the two data normalisation types, with the z-score normalisation providing higher DC values over all land cover classes, except for Forests.

When not only Sentinel-1 but also Sentinel-2 data were fed to the CNN, the BA classification did not improve (except for Crops) in comparison to only using Sentinel-2 data, despite requiring more computation time in all configurations. Over cropping areas, SAR or optical data alone provided a low mapping accuracy (highest DCs achieved 0.37±0.14 and 0.42±0.05, respectively). However, the SAR-O combination improved the accuracy (DC 0.44±0.09) by reducing the OE. Such an improvement was maximum for the 2D convolution and z-score normalisation. For the remaining land cover classes, the SAR and optical combination did not improve the results when cloud cover was not an issue. Despite Sentinel-2 temporal compositing, gaps remained over areas frequently affected by clouds. As for the CNN optimum configuration, 1D convolution and [0, 1] normalisation improved the mapping accuracy (as for the Sentinel-1 based network). The highest mapping accuracy was observed over Forests regardless of the data normalisation method, convolution dimension and input remote sensing data (i.e., S-1, S-2, S-1 + S-2). The optimum CNN configuration for each land cover class is presented in Table 4 as a function of the input remote sensing data.

The softmax layer (i.e., the last layer of the CNN) predicted the probability that each pixel would have been burned or unburned.

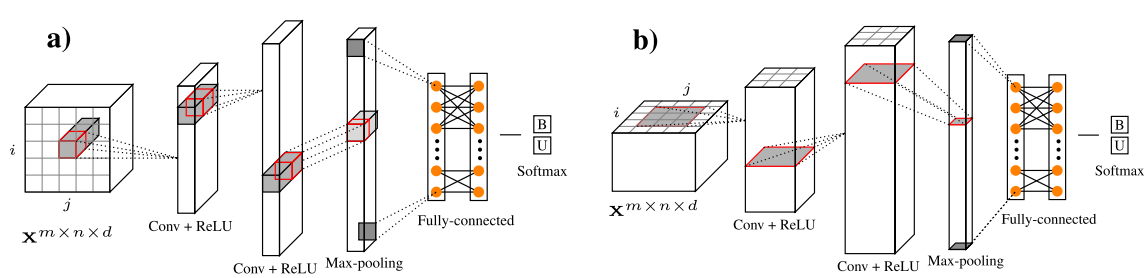

Fig. 4. Feature extraction carried out in a convolution (Conv) through (a) the spectral-domain (1D) and (b) the spatial-domain (2D) of the input image. Relevant parts of CNN such as ReLU, max-pooling, fully-connected network and softmax layers are also shown.

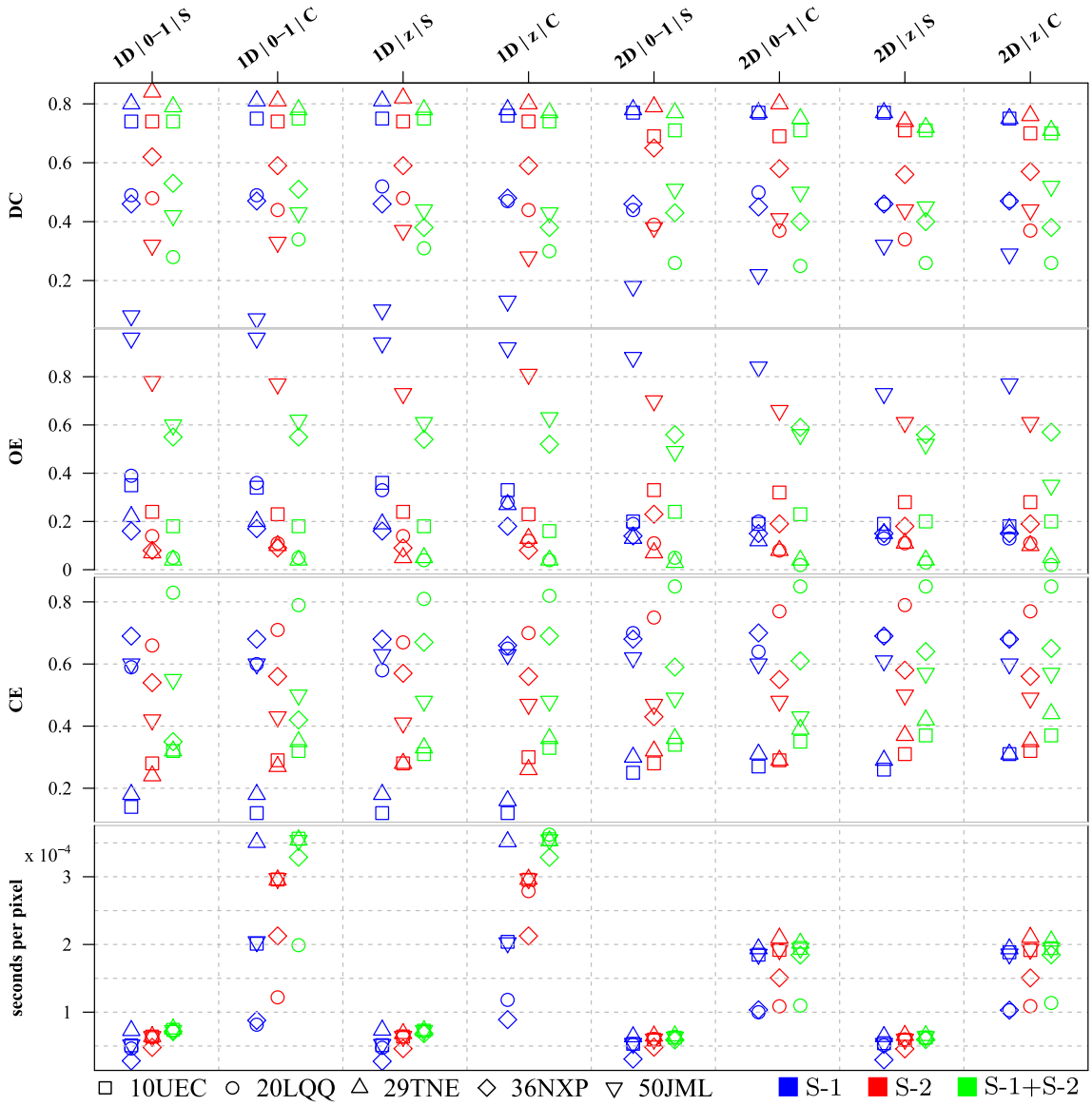

Fig. 5. Dice coefficient (DC), commission and omission errors (CE and OE) and seconds needed when training the models by training tiles considering different CNN configuration and input data (Sentinel-1 - S-1, Sentinel-2 - S-2 and both datasets - S-1 + S-2).

Although in our previous analysis, pixels were classified as burned when such a probability was equal to or above 50%, such a fixed threshold, based on a statistical proxy instead of on the data analysis, may not provide the optimum performance. Hence, we analysed the use of a variable probability threshold to improve the BA mapping accuracy, balancing CE and OE (Fig. 7). Such variation depended on the land cover class and the input data fed to the CNN (Table 5). Over Grasslands, Crops and Shrubs (i.e., the classes with the highest OE (Fig. 6)) accuracies improved when the softmax burned probability threshold was reduced (40 to 50%), although it depended on the input data. Conversely, for the Forests class, a more restrictive threshold improved the classification. The optimum threshold differed with the input data, from 65% when using Sentinel-2 data alone to 75% when using Sentinel-1 or integrating SAR and optical data. BA accuracy improved marginally for the Others class when varying the threshold until a probability of 80% for Sentinel-1 and 70% for Sentinel-2. However, when integrating SAR and optical data, the improvement was considerable for the 55–75% interval, with the highest accuracy achieved for a softmax threshold of 70%. Such an improvement allowed that maps based on SAR-O integration had higher accuracy when compared to those derived from individual Sentinel-1 or Sentinel-2 datasets. Past the optimum threshold, mapping accuracy reduced considerably, especially when using Sentinel-2 data. This effect was observed for all land cover classes except for Grasslands.

4.2. SAR-optical mapping strategy

Three different BA mapping strategies when combining SAR and optical datasets were analysed: (i) stacking radar as well as optical data (i.e., backscatter coefficient, optical surface reflectances and spectral indices) and feeding them to the CNN (Fig. 8, a), (ii) using BA detected from the optical data and filling the cloud cover-induced gaps with pixels mapped from radar data (Fig. 8, b) and (iii) joining the BA detected independently from radar and optical datasets (Fig. 8, c). For the Forests class, the three mapping strategies provided similar results (i.e., DC values). However, joining individual Sentinel-1 and Sentinel-2 maps may provide an advantage by reducing missed burned pixels due to clouds or shadows, not possible when using optical temporal composites alone. For Shrubs, the observed DC values were similar for all mapping strategies, with radar-filled optical-based BA maps showing slightly higher DC values when compared to the remaining two

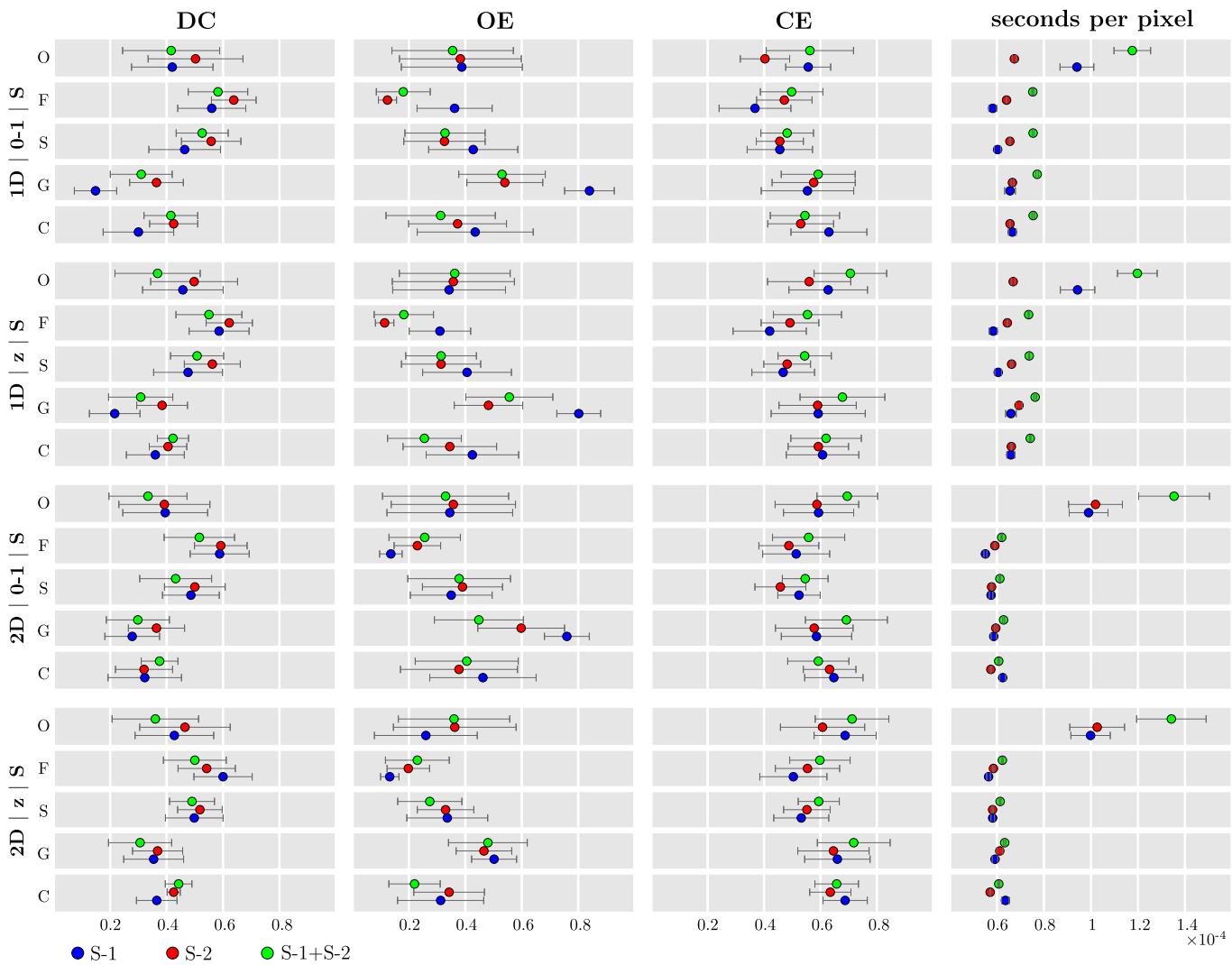

Fig. 6. Mean and standard error of Dice coefficient (DC), commission and omission errors (CE and OE) and seconds per pixel needed when training the models by land cover classes (O-others, F-forests, S-shrubs, G-grasslands and C-crops) of training tiles considering different CNN configuration and input datasets (Sentinel-1 - S-1, Sentinel-2 - S-2 and both datasets - S-1 + S-2).

Table 4
Optimum CNN configuration and Dice coefficient mean (± standard deviation) by land cover classes (O-others, F-forests, S-shrubs, G-grasslands and C-crops) of the training tiles and input datasets (Sentinel-1 - S-1, Sentinel-2 - S-2 and both datasets - S-1 + S-2).

LC	S-1	DC (S-1)	S-2	DC (S-2)	S-1+S-2	DC (S-1+S-2)
O	1D | z-score	0.46±0.31	1D | z-score	0.50±0.31	1D | [0, 1]	0.42±0.38
F	2D | z-score	0.60±0.23	1D | [0, 1]	0.64±0.21	1D | [0, 1]	0.58±0.24
S	2D | z-score	0.50±0.23	1D | z-score	0.56±0.22	1D | [0, 1]	0.53±0.20
G	2D | z-score	0.35±0.24	1D | z-score	0.38±0.20	all	0.31±0.23
C	2D | z-score	0.37±0.15	2D | z-score	0.43±0.19	2D | z-score	0.44±0.11

strategies. Over Grasslands, the radar-filled optical-based BA maps provided the most accurate results. Over the two remaining land cover classes (i.e., Others and Crops), using radar-optical stacked data into the CNN allowed improving the accuracy. In particular, over the Others class, the radar-optical stacks allowed reducing the CE by 20%.

4.3. Burned area mapping validation

The optimum CNN configuration and mapping strategy, according to the observed trends over the training tiles, were assessed over the test tiles (Table 6) with the mapping accuracy varying depending on the input data (i.e., S-1, S-2 and S-1 + S-2). Higher mapping errors (DC<0.6) were observed over grasslands dominated tiles in Africa and Australia (33NTG and 52LCH, respectively), regardless of the input data. Over the remaining tiles, DC values were above 0.7. Over two tiles (20LQP and 33NTG), the radar-based maps were more accurate when compared to the optical-based (DC of 0.81 vs 0.71 and 0.50 vs 0.47, respectively) with the opposite being valid for the remaining three tiles. However, the use of Sentinel-1 data (i.e., cloud cover independent) allowed for wall-to-wall mapping. In tile 52LCH the optical-based maps did not provide information for 17.6% (Fig. 9).

By land cover type, the highest accuracy was observed over forested areas when mapping BA through the SAR-O combination (DC 0.72) as opposed to only using SAR (DC 0.63) or optical (DC 0.66) information (Fig. 10). The most relevant improvement when combining Sentinel-1 and Sentinel-2 was found over the Others class, where the synergy of both sensors reduced OE and CE considerably. The lowest accuracy was achieved over the Crops class, mainly due to high CE (near 0.8) observed for both sensor types. In addition, for the radar-based maps, BA accuracy

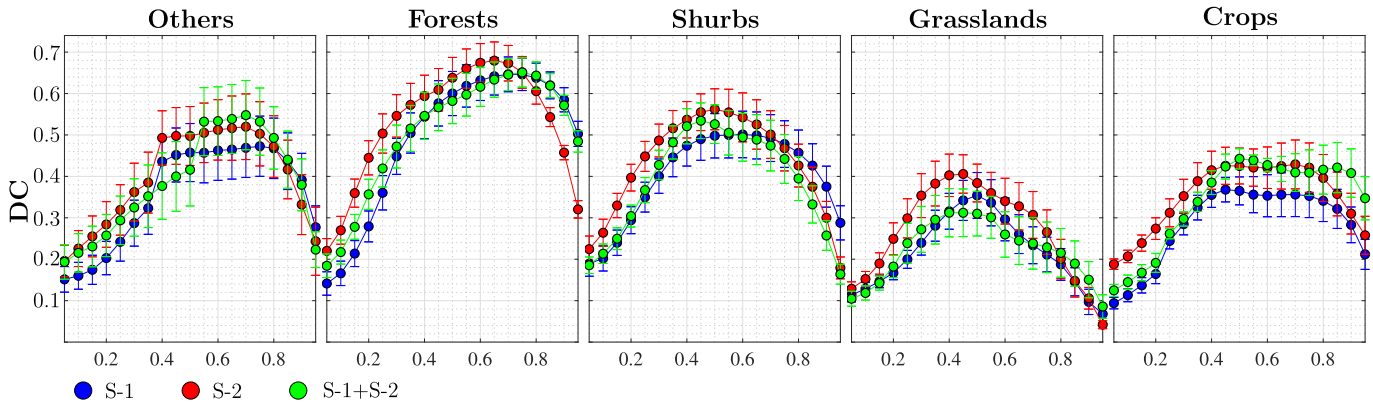

Fig. 7. Variation of mapping accuracy measured through the mean and standard error of Dice coefficient (DC) as a function of changes in softmax probability by land cover classes of training tiles and input datasets (Sentinel-1 - S-1, Sentinel-2 - S-2 and both datasets - S-1 + S-2).

Table 5
Most suitable burned thresholds (Bt) of softmax classification probability layer when mapping burned area (BA) and the mean Dice coefficient (± standard deviation) by land cover classes (O-others, F-forests, S-shrubs, G-grasslands and C-crops) of training tiles and input datasets (Sentinel-1 - S-1, Sentinel-2 - S-2 and both datasets - S-1 + S-2).

LC	Bt (S-1)	DC (S-1)	Bt (S-2)	DC (S-2)	Bt (S-1+S-2)	DC (S-1+S-2)
O	0.75	0.47±0.32	0.70	0.52±0.35	0.70	0.55±0.36
F	0.75	0.65±0.17	0.65	0.68±0.20	0.75	0.65±0.15
S	0.55	0.50±0.24	0.50	0.56±0.22	0.45	0.53±0.19
G	0.50	0.35±0.24	0.45	0.41±0.20	0.40	0.31±0.25
C	0.45	0.37±0.13	0.50	0.43±0.19	0.50	0.44±0.11

over cropping areas was also negatively influenced by high OE, which did not occur when using optical datasets. The combination of Sentinel-1 and Sentinel-2 data generally improved or maintained the accuracy achieved from individual datasets except for tile 20LQP, where the SAR-based maps were the most accurate. When combining the two sensor types, we observed a considerable reduction in OE which coupled with a marginal increase in CE. The average OE reduction and CE increment over the five test tiles was 0.22±0.22 and 0.05±0.17 as well as 0.09±0.08 and 0.05±0.05 when compared to radar- and optical-based maps, respectively. Apart from accuracy improvements, SAR-O data integration reduced gaps due to cloud cover to nil, a significant advantage of combining active and passive sensors.

5. Discussion

5.1. Optimum CNN parameters

Optimum CNN parameters were proposed based on the five training tiles and applied to the test tiles (Fig. 1). The training-test tiles are geographically distributed and exhibit considerable differences in land cover distribution, FRP and soil moisture that might affect BA mapping accuracy (Table 1). Nevertheless, no significant variations were observed between the BA mapping accuracies achieved over the training and test tiles. It may be explained by the use of local CNN training, which

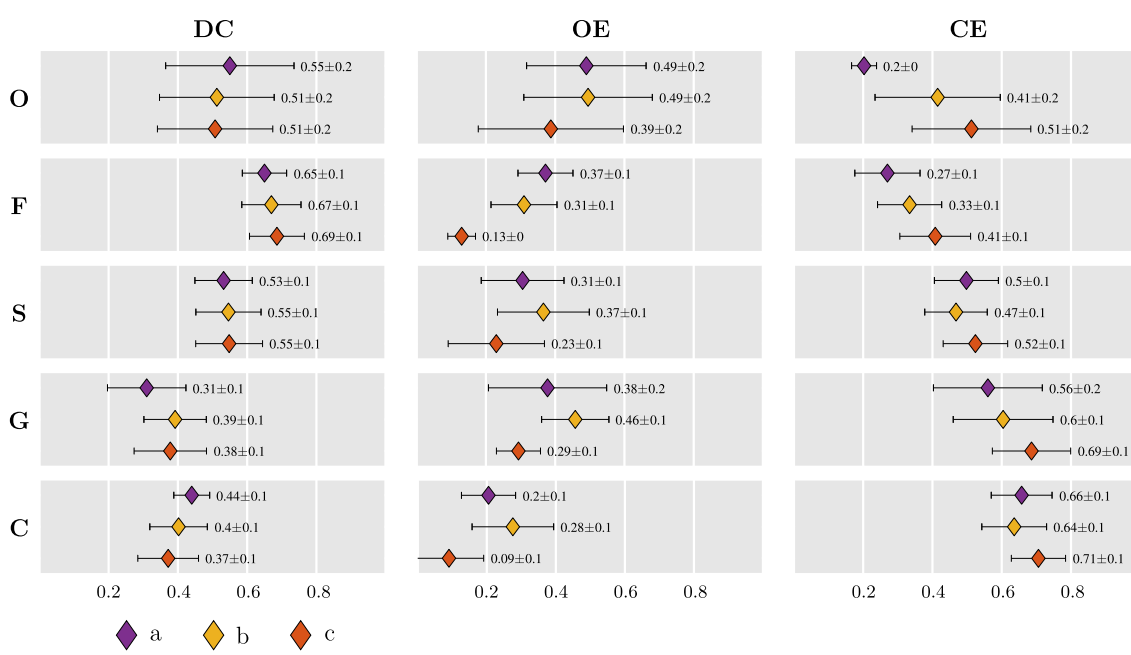

Fig. 8. Mean and standard error of Dice coefficient (DC) and commission and omission errors (CE and OE) by land cover classes (O-others, F-forests, S-shrubs, G-grasslands and C-crops) of training tiles when combining Sentinel-1 and Sentinel-2 data applying three different approaches: (a) data stacking of SAR and optical images to feed the CNN; (b) filling Sentinel-2 based maps pixels with information-gaps using those derived from Sentinel-1; and (c) joining all burned pixels detected using both SAR and optical images separately.

Table 6
Error metrics for burned area (BA) maps based on Sentinel-1 (S-1), Sentinel-2 (S-2) and the optimum combination of both datasets (S-1 + S-2) for each test tile.

MGRS	C	Reference period	Sat	Detection period	DC	OE	CE	%Nd
10SEH	NA	04/10/2017–05/11/2017	S-1	28/09/2017–03/11/2017	0.46	0.69	0.13	0.00
			S-2	07/10/2017–01/11/2017	0.70	0.12	0.41	2.26
			S-1 + S-2	28/09/2017–03/11/2017	0.70	0.10	0.43	0.00
20LQP	SA	20/07/2016–22/09/2016	S-1	03/07/2016–25/09/2016	0.81	0.08	0.27	0.00
			S-2	17/07/2016–25/09/2016	0.71	0.20	0.37	0.00
			S-1 + S-2	03/07/2016–25/09/2016	0.73	0.04	0.41	0.00
29TNG	Eu	05/10/2017–06/11/2017	S-1	28/09/2017–09/11/2017	0.64	0.44	0.25	0.00
			S-2	05/10/2017–09/11/2017	0.75	0.27	0.22	0.06
			S-1 + S-2	28/09/2017–09/11/2017	0.77	0.23	0.22	0.00
33NTG	Af	15/01/2016–16/02/2016	S-1	15/01/2016–20/02/2016	0.50	0.53	0.47	0.00
			S-2	18/01/2016–/17/02/2016	0.47	0.65	0.31	0.39
			S-1 + S-2	15/01/2016–20/02/2016	0.56	0.47	0.42	0.00
52LCH	Au	05/04/2017–21/04/2017	S-1	26/03/2017–19/04/2017	0.36	0.75	0.34	0.00
			S-2	19/03/2017–08/04/2017	0.55	0.59	0.15	17.6
			S-1 + S-2	26/03/2017–19/04/2017	0.56	0.55	0.24	0.00

C - continent for each tile (Af-Africa, Au-Australia, Eu-Europe, NA-North America and SA-South America); Reference period - period for which it was derived the reference burned perimeters using Landsat-8; Sat - input dataset considered; Detection period - first and last Sentinel-1 or Sentinel-2 images of the temporal series; DC - Dice coefficient; OE - omission error; CE - commission error; and %Nd - the percentage of no data pixels over all the MGRS tile.

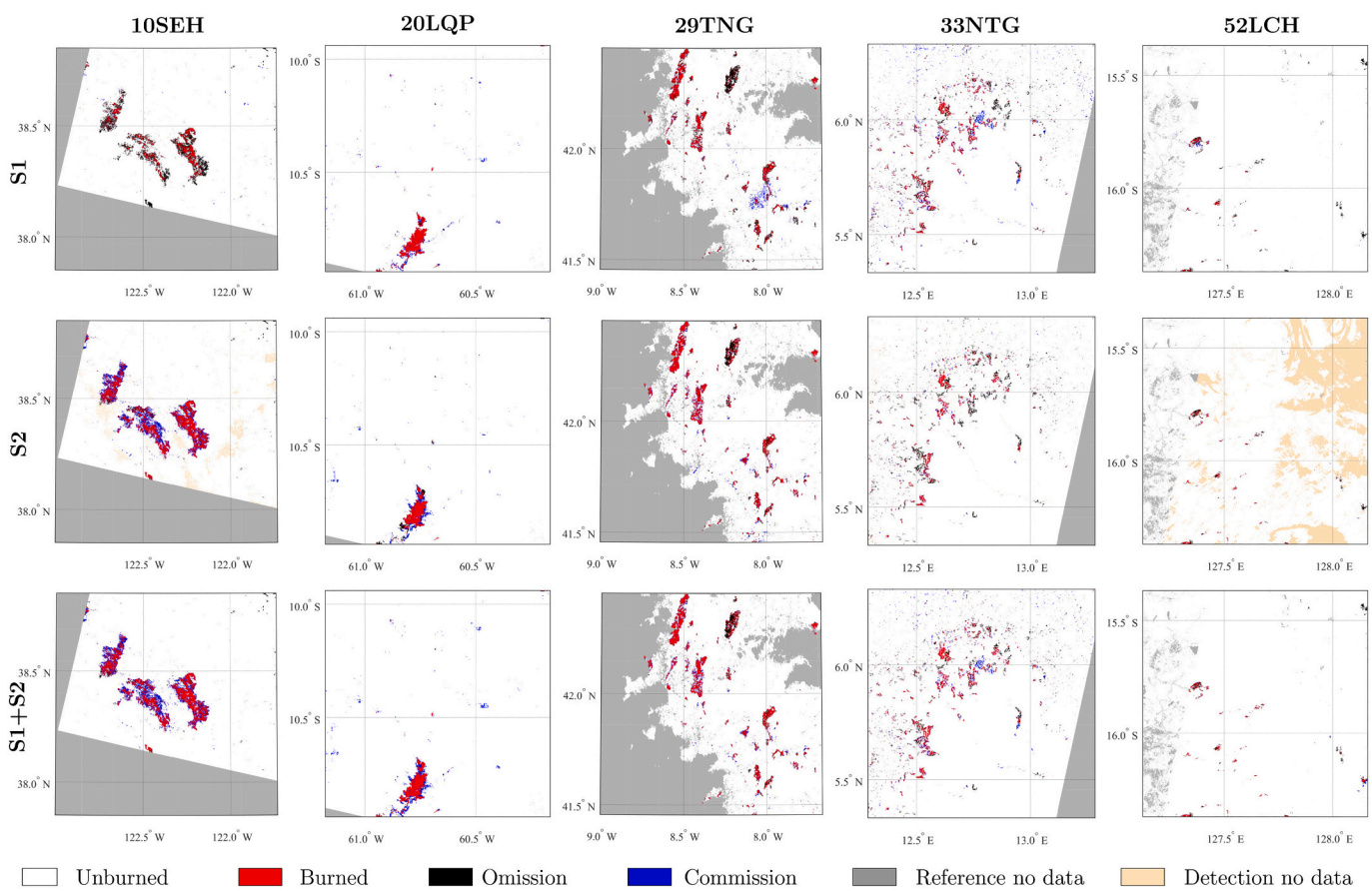

Fig. 9. Burned area (BA) maps based on Sentinel-1 (S-1), Sentinel-2 (S-2) and the optimum combination of both datasets (S-1 + S-2) for the test tiles. Errors of omission and commission, as well as no data pixels due to reference or input datasets are also shown.

provided a representative set of optimum parameters.

Our results show that the optimum data normalisation was based on the z-score when using either radar or optical data as input. The only exception was for forested areas mapped from Sentinel-2 imagery, which aligns with findings from previous research (Zhong et al., 2017). Conversely, when using a combined SAR-O dataset, the [0, 1] normalisation was better suited for mapping applications, as also observed in previous studies that combined imagery from these sensors (Benedetti et al., 2018a). The [0, 1] normalisation provided more accurate BA detections when stacking SAR and optical datasets except for Grasslands (no difference with z-score normalisation) and Crops. For Grasslands, the insensitivity to the normalisation method may be related to the low BA mapping accuracies. On the other hand, for Crops, the intrinsic class vegetation differences given by the variability of different agricultural fields as well as the vegetation season may explain the need for a different normalisation type.

The optimum feature extraction was achieved via the spectral domain (1D) when the optical or the SAR-O combination was used.

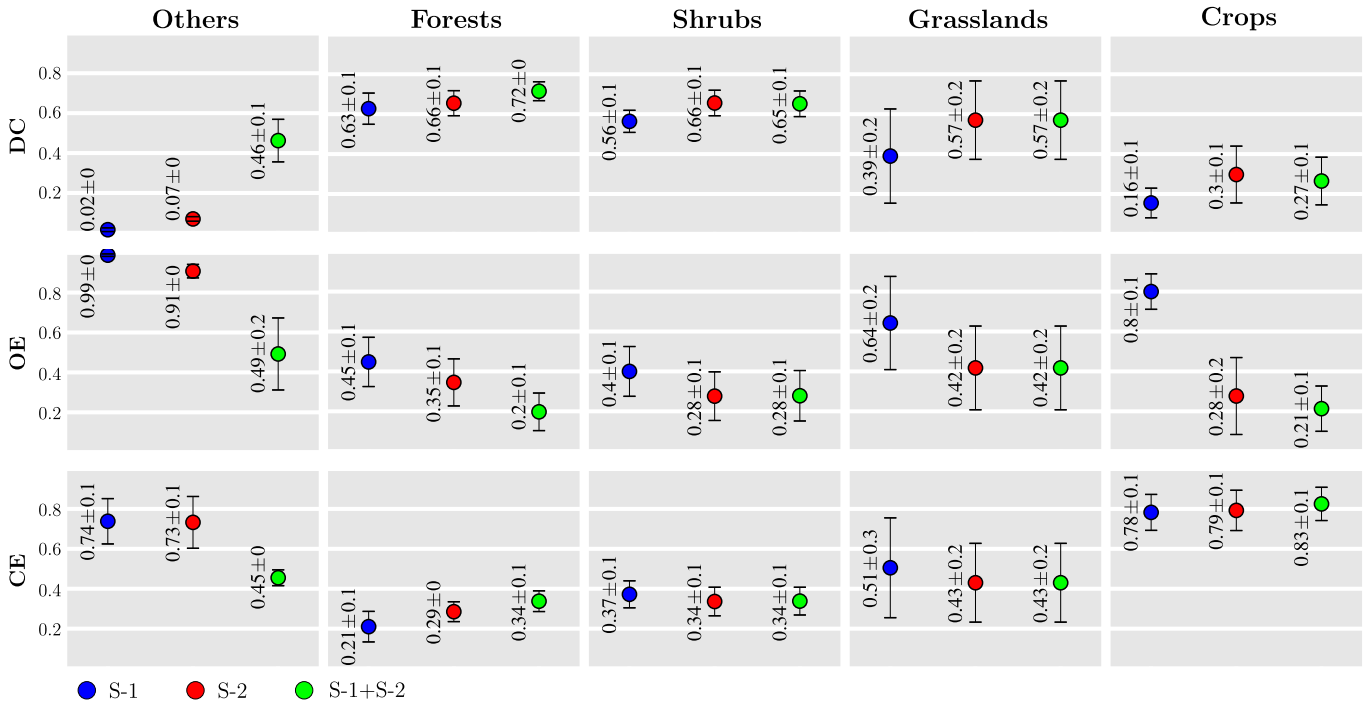

Fig. 10. Mean and standard error of Dice coefficient (DC), commission and omission errors (CE and OE) by land cover classes of test tiles as a function of the input datasets used (Sentinel-1 - S-1, Sentinel-2 - S-2 and the optimum combination of both datasets - S-1 + S-2).

Conversely, the spatial domain (2D) provided more accurate results when using SAR data alone. Such a difference may be due to optical reflectances allowing mapping BA better than the radar backscatter coefficient data (Belenguer-Plomer et al., 2019c). Hence, only considering the spectral reflectances of those wavelengths highly sensitive to fire effects results in accurate classification of BA. However, when only the backscatter coefficient is available, considering the surrounding pixels improves the differentiation between burned and unburned, which explains the improved performance of the spatial feature extraction.

The optimum Softmax threshold, when distinguishing between burned and unburned pixels, differed as a function of land cover classes. The most considerable enhancement, when varying the threshold from 50% was observed for the Others class, which was mapped more accurately when considering SAR-O using a 60% probability threshold. The optimum thresholds also varied as a function of the input data (SAR, optical or SAR-O combination) over each land cover class. For Crops, Grasslands and Shrubs, the optimum thresholds were less restrictive (i.e., close to 50%), while for Forests and Others classes, the optimum ones were more restrictive (i.e., around 70%). Except for Shrubs, a higher threshold (for BA detection) seemed appropriate for the land cover classes mapped with higher accuracy (i.e., Forests and Others). These thresholds have been defined considering a reduced number of study areas so that further research is needed to confirm them. Nevertheless, the broad range of terrestrial ecoregions, land cover classes, fire radiative power as well as soil moisture and precipitation patterns observed over the training sites (Table 1) suggest their utility over a wide array of conditions and their transferability to other areas. The higher mapping accuracy may be related to the biomass level of each land cover class as it influences the level of pre- to post-fire changes for both, the backscatter coefficient and optical reflectance. In addition, the Fire Radiative Power (FRP) is dependent on fuels availability (i.e., biomass) which implies that in land cover classes with a reduced amount of biomass, the capability to detect hotspots from thermal sensors is lower when compared to land cover classes with a higher quantity of biomass (Wooster et al., 2005). CNN models are land cover dependent and trained using information derived from hotspots. Hence, a reduced number of hotspots for a specific land cover class (e.g., due to low FRP or related to low biomass levels) resulted in suboptimal training, and as such, increased the uncertainty when compared to land cover classes with higher fuel availability, and consequently hotspots, which indeed explains the different optimum thresholds for each land cover class.

Lastly, in terms of computing time, mapping the BA over a vegetation class with considerable intrinsic heterogeneity (i.e., Others class) increased the computing duration. However, the most significant time increment was found when using additional hidden layers which did not translate into mapping accuracy improvements. Although including more hidden layers does not deteriorate the mapping accuracy, the considerable increase of computing time may hinder algorithm deployment from continental to global scales, the final objective of this research (Chuvieco et al., 2019).

5.2. SAR and optical data integration for BA mapping

The input data (SAR, optical, joint use) providing the highest accuracy differed with the land cover class. For Others and Crops classes, the joint use of active and passive data provided the most accurate results. As these land cover classes are more heterogeneous, the mapping process takes advantage of the different sensitivity of the two types of sensors through the CNN training, allowing for a more precise separation between burned and unburned areas overall. Notice that over the test tiles, the joint use of both sensor types did not improve results for the Crops class, which suggests that further research is needed to ascertain the optimum combination of active and passive datasets. A possible explanation is a reduced variability among the types of crops within the test tiles. Such reduced variability was suggested by the reduced VH backscatter coefficient variability (i.e., standard deviation), related to the vegetation volumetric scattering process (Freeman and Durden, 1998), over the Crops in the test tiles when compared to the training ones (0.10 vs 0.15). Increased homogeneity over the agricultural fields, induced by different crop types and/or growing seasons, may reduce the need for SAR-derived information for monitoring purposes (Van Tricht et al., 2018). Nevertheless, comparing SAR-O and optical-based results over the test tiles suggest only marginal DC differences over cropping

areas and demonstrates the reliability of the CNN-based predictions, even when some of the input data are redundant.

For Forests and Shrubs classes, the combination of BA mapping products based on either individual SAR or optical data sources allowed for more accurate detections; however, such improvements were marginal, especially for Shrubs, when compared to the remaining data-integration strategies. The improvement resulted from a considerable OE reduction when joining the independently generated maps. In particular, OE was reduced for pixels located at the border of fire patches which are more susceptible to be misclassified due to residual pixel co-registration errors between maps and validation datasets (Mandanici and Bitelli, 2016). Hence, combining maps obtained from sensors with different viewing geometries (i.e., SAR and optical) reduced the geo-location error effect without meaningfully increasing the CE. Lastly, over Grasslands, the use of Sentinel-2 data for BA mapping and Sentinel-1 for cloud-induced gap-filling provided the most accurate results. Such findings align with previous research which suggested reduced utility of C-band backscatter coefficient when monitoring fire effects in fire-affected grasslands (Menges et al., 2004).

5.3. Algorithm independent validation

The joint use of Sentinel-1 and Sentinel-2 data improved slightly or at least maintained the BA accuracy achieved using a sole input data (i.e., SAR or optical) in most test tiles while providing wall-to-wall mapping capabilities (i.e., all pixels were mapped), a feature particularly crucial in tile 52LCH, were cloud-induced gaps amounted to 17.6% of the area. Further, the joint use of active and passive datasets allowed combining the strengths of SAR (i.e., a cloud cover independence) and optical data (i.e., better sensitivity to fire-induced changes in vegetation) as also suggested in previous studies (Verhegghen et al., 2016). As an exception, for tile 20LQP, the highest accuracy was obtained using the SAR data (DC 0.81). The OE increased by 0.2 when using Sentinel-2 data as an input and by 0.04 when jointly using the active and passive datasets. However, for the latter, the CE significantly increased when joining all burned pixel detected separately from SAR and optical datasets due to the large commission errors of the Sentinel-2 based maps. The discrepant results in tile 20LQP were explained by fire location, as 83% of the fire patches burned forested areas and did not reflect the general trends as discussed in Section 5.4. Overall, using SAR and optical data for BA mapping requires more computing power or increased processing time. However, such an effort may be worth it whether end-users are provided with the most accurate BA products without information gaps, particularly beneficial at inter-tropical latitudes.

By land cover classes, the higher mapping accuracies were observed for Forests, Shrubs and Grasslands with DC values of 0.72, 0.65 and 0.57, respectively. A lower DC value (0.46) was observed for the Others class whereas a rather low mapping accuracy was observed for Crops (DC 0.27) regardless of the input datasets. However, one should notice that most accuracy metrics were based on reference fire perimeters over short periods (i.e., one month or less), which may significantly affect accuracy assessment. According to previous research, evaluating BA maps over short periods tends to underestimate mapping accuracy regardless of the input datasets (Padilla et al., 2018). Such effects were also found when assessing Sentinel-2 based BA maps with DC values increasing from 0.34 to 0.77 from short to long temporal periods (Roteta et al., 2019).

In this study, most of the evaluated periods were short. However, two clearly defined groups of tiles were observed when analysing the BA mapping accuracy from Sentinel-2 data. For the first group, formed by tiles 10SEH, 20LQP and 29TNG, the fire activity was concentrated around dates timely covered by both the reference (as set by Landsat 8 acquisition dates) and the detection period (set by the Sentinel-2 acquisition dates). Over these tiles, the DC values were similar (DC >0.7) and in line with those observed in previous studies (Roteta et al., 2019). For the second group, tiles 33NTG and 52LCH, many fires were active during dates not simultaneously covered by Landsat-8 and Sentinel-2 acquisitions. In fact, 8.8% (33NTG) and 39.4% (52LCH) hotspots were recorded within the interval covered by the Lansat-8 imagery (16 days revisit period) but outside the interval covered by the Sentinel-2 ones (5 days revisit period). Such a mismatching may explain the increased OE (0.65 and 0.59, respectively) and thus the lower accuracy as the average DC was lower (0.21) when compared to the remaining tiles (DC 0.51 vs 0.72).

The accuracy observed for the Sentinel-1 based BA maps was similar to that observed in previous studies based on the same sensor (Belenguer-Plomer et al., 2019c). For the test tiles, the CNN-based maps achieved an average DC of 0.55 ± 0.17 while the Reed-Xiaoli detector-based approach proposed by Belenguer-Plomer et al. (2019c) achieved 0.57 ± 0.18. Although only marginal differences, in terms of accuracy, were found between the two approaches, the CNN-based algorithm was considerable faster (Belenguer-Plomer et al., 2019c). Regarding the combination of active/passive derived data, the reduced number of studies that took advantage of such a fusion when mapping BA mapping precluded meaningful comparisons as such studies were carried out over homogeneous areas with little variations in vegetation types and fire regimes (Verhegghen et al., 2016; Brown et al., 2018; Stroppiana et al., 2015).

5.4. Main sources of error

BA mapping commission and omission errors depended, to a large degree, on the input data source. SAR and optical datasets were affected differently by factors including variations in soil moisture, slope orientation and post-fire vegetation response (Kurum, 2015; Belenguer-Plomer et al., 2019a). For tile 10SEH (North America), the main limiting factor when using SAR data was the steep topography since fire patches were located on steeper slopes ($13.46^{\circ}\pm7.7$) when compared to the remaining test tiles ($7.15^{\circ}\pm6$). The steep topography may reduce the backscatter suitability when monitoring fires, which translates into increased OE (0.69) (Belenguer-Plomer et al., 2019c). Conversely, considerable CE (0.41) was observed for the optical-based maps as during the automatic training low-fire severity pixels (i.e., reduced pre- to post-fire variations) were considered due to their distance to hotspots. However, the reference perimeters only included visible burned pixels since their generation was based on a manually supervised classification. The mean dNBR, a reliable indicator of fire severity (Key and Benson, 2004), in pixels affected by CE was 0.15 ± 0.16, a value considerably higher when compared to that of unburned pixels (0.01 ± 0.7) and, at the same time, far from the values observed for the accurately mapped burned pixels (0.46 ± 0.26). Hence, it is thought that had the reference perimeters included partially burned pixels as burned, the CE would have been lower.

Fire severity was also the main limiting factor in tiles 33NTG (Africa) and 52LCH (Australia). According to the MIRBI spectral index (Eq. (4)), found as the most suitable index when assessing fire severity over grasslands (Lu et al., 2016), low fire severity was observed for pixels affected by OE (1.67 ± 0.38 and 1.62 ± 0.21, respectively). In contrast, moderate severities were noticed for accurately detected burned pixels (1.8 ± 0.32 and 1.76 ± 0.12, respectively). Although marginal differences were found when comparing accuracies from SAR-O and optical-based maps (DC 0.56 vs 0.55, respectively), when evaluating the accuracy of the latter, pixels covered by clouds (17.6%) were not included despite some of them were affected by fires. In fact, whether these cloud-covered pixels are ignored when assessing the SAR-O BA map in tile 52LCH, the accuracy improves up to 12.5% (DC 0.63). Furthermore, as indicated in Section 5.3, mismatched reference and detection periods may have increased the observed errors (particularly OE) in tiles 33NTG and 52LCH.

Hotspots availability may have also affected the observed mapping accuracy. For example, in tile 29TNG (Portugal), most areas affected by omission errors were located within a unique fire scar with only one

hotspot detected by the thermal MODIS and VIIRS sensors. The reduced number of hotspots hindered the CNN training for SAR, optical and both combined datasets. However, the absence of hotspots was an exception since not only within the remaining fire patches of the same area but also in the rest of the tiles such limitations were not observed.

Regarding the high CE observed in tile 20LQP (South America), particularly for the optical-based map (0.37), it was related to a similar post-fire increment in SWIR reflectance over both burned (+0.046) and unburned (+0.05) areas. The SWIR increment over unburned areas may be related to drying unburned vegetation during the post-fire period (Gao, 1996). Most pixels (77%) affected by CE were spatially concentrated along the largest fire perimeter, a fire that accounted for 93.3% of all burned pixels in this tile. According to the MODIS-based hotpots product (Giglio et al., 2016), FRP values up to 339.9 MW were observed for this fire, a 15th fold increase when compared to value registered over the remaining fire-patches (20.3 MW), which suggests that heat radiating from the very intense fire-affected vegetation on the neighbouring areas. As CNN training was based on larger areas around hotspots, unburned fire-dried pixels were mixed within the training burned samples, which resulted in an incorrect learning process. Such errors may be easily rectified by relating the sampling areas around hotspots with the FRP (i.e., being sampled within a lower radius around the hotspots the burned training pixels from intense fires). Soil moisture variations may affect the BA mapping accuracy when considering SAR data (Imperatore et al., 2017; Gimeno and San-Miguel-Ayanz, 2004; Ruecker and Siegert, 2000). However, in this study such an effect has not been observed as the recorded variations of soil moisture between pre- and post-fire images occurred in the entire scene (i.e., a background change). When soil moisture changes are concentrated in smaller regions, as a result of a focused rainfall, misclassification may occur and translate into increased CE (Belenguer-Plomer et al., 2019c). However, despite the reliability of the SMAP product (Chan et al., 2018; Chen et al., 2018), its coarse spatial resolution (i.e., 9 km) does not allow monitoring spatially concentrated changes. Thus, soil moisture effects on SAR-based BA mapping may have been underestimated. Further analysis considering a more spatially detailed product of soil moisture is needed. However, to date, the most spatially detailed soil moisture product, the Copernicus Surface Soil Moisture (SSM) at 1 km based on Sentinel-1 data, is only available over Europe (Bauer-Marschallinger et al., 2018) precluding a more in-depth analysis over most of our study sites.

5.5. Further research and improvements

This research has advanced the current state-of-the-art in BA mapping using both radar and optical sensors of medium spatial resolution. The unprecedented scenario in which (i) Sentinel-1 and -2 data free distribution under the European Copernicus programme as well as (ii) the recent advances in deep learning algorithms (e.g., CNN) have allowed investigating novel BA detection and mapping techniques as the proposed one. The presented algorithm has the potential to reduce uncertainties on current BA products, estimated at 4 to 4.5 million km^2 globally (Giglio et al., 2018; Lizundia-Loiola et al., 2020). However, in order to confirm the global relevance of these findings, further research is needed to include additional study sites over all the fire-prone biomes. To this end, a recently published Burned Area Reference Database (BARD), based on 2769 images acquired by Landsat-7 and -8 and Sentinel-2 satellites (Franquesa et al., 2020), would be hugely beneficial to validate the proposed algorithm.

As soil moisture changes the importance of C-band VV and VH polarisations when distinguishing between burned and unburned areas (Van Zyl et al., 2011; Belenguer-Plomer et al., 2019a, 2019b), BA mapping based on Sentinel-1 datasets shall take into account more reliable information on soil moisture as ancillary global products become available at higher spatial resolutions. Current global products (i.e., SMAP at 9 km or CCI soil moisture at 0.25°) are not accurate enough for such purposes. In particular, future iterations may assign differentiated weights for the VV and VH polarisations based on soil moisture information as VV importance for BA mapping increases with soil moisture (Belenguer-Plomer et al., 2019a). Further improvements may be achieved by stratifying the training pixels based on the fire radiative power (related to fire intensity). Such an approach may reduce the increased uncertainties observed over areas affected by low fire intensities (i.e., low FRP), which results in reduced fire severity, an important factor affecting BA accuracy (Tanase et al., 2014; Belenguer-Plomer et al., 2019c). Such a stratification may improve CNN training and thus reduce CE and OE for approximately 15% of the burned pixels with no recorded hotspots in the close vicinity. Finally, BA mapping within the proposed framework may greatly benefit from the concurrent use of different SAR wavelengths such as L- (from the future NISAR mission, launch planned in 2021) and P-band (from the future Biomass mission, launch planned in 2022). Adding longer wavelength may allow for discriminating surface fires in forested areas, difficult to be detected from optical and shortwave SAR wavelengths such as C-band.

6. Conclusions

This study provides insights for the optimum configuration, by land cover class, of CNN algorithms fed by Sentinel-1 and/or Sentinel-2 datasets when detecting and mapping burned area. The analysis was carried out over 10 study areas (1 M ha each) distributed within a broad range of terrestrial ecoregions, with diverse land cover classes, affected by different fire intensities and environmental conditions (i.e., soil moisture and precipitation patterns). CNN models with two hidden layers allowed reducing the computing time with virtually no loss in maintaining mapping accuracy when compared to deeper networks regardless of the input data (i.e., Sentinel-1, Sentinel-2 and both) or the observed land cover class. Three factors were relevant when defining an optimum CNN configuration: (i) the dimension where the convolution-based feature extraction was executed (i.e., spectral or spatial), (ii) the data normalisation method (z-score or interval [0, 1]), and (iii) the optimum threshold of the softmax output layer. In addition, the land cover class was relevant when defining the most accurate SAR-O data integration strategy.

The optimum CNN parameters were used to map BA over five independent test areas, not used for algorithm optimisation, with similar accuracies when compared to those achieved over the training tiles. The consistent behaviour, despite using geographically distributed sites, was possible due to a local model training approach supported by the thermal anomalies. Error analysis over the test tiles suggested a strong relationship between mapping accuracy and the land cover classes, as observed in previous studies. The highest and lowest accuracies were found over Forests and Grasslands, respectively. When individual data were fed into the CNN (i.e., Sentinel-1 or Sentinel-2), the observed mapping accuracies were similar to those found in the literature. However, the proposed CNN approach was considerably more versatile with respect to the existing BA mapping algorithms. Besides, this study provided insights into the optimum SAR-O data integration, which allows (i) improving BA mapping accuracy when compared to using a single sensor type and (ii) wall-to-wall mapping as cloud-related gaps affecting BA products from optical datasets were eliminated. Despite these strengths, CNN-based BA mapping accuracy was limited by different sources of errors including steep topography, low FRP, absence of hotspots and presence of fire unrelated land changes. Future research should consider more study areas from representative fire-prone biomes to confirm the relevance of these findings.

Declaration of Competing Interest

The authors declare no conflict of interest.

Acknowledgements

This research has been financed by the (i) Spanish Ministry of Universities through a Formación Profesorado Universitario (FPU) doctoral fellowship (FPU16/01645) and its mobility grant associated (EST18/00497) as well as (ii) by the European Space Agency (ESA) through the Fire_cci (Climate Change Initiative) project (Contract 4000126706/19/I-NB).

References

Agostinelli, F., Hoffman, M., Sadowski, P., Baldi, P., 2014. Learning Activation Functions to Improve Deep Neural Networks arXiv preprint arXiv:1412.6830.
Anantrasirichai, N., Biggs, J., Albino, F., Bull, D., 2019. A deep learning approach to detecting volcano deformation from satellite imagery using synthetic datasets. Remote Sens. Environ. 230, 111179.
Aponte, C., de Groot, W.J., Wotton, B.M., 2016. Forest fires and climate change: causes, consequences and management options. Int. J. Wildland Fire 25 i–ii.
Ban, Y., Zhang, P., Nascetti, A., Bevington, A.R., Wulder, M.A., 2020. Near real-time wildfire progression monitoring with Sentinel-1 SAR time series and deep learning. Sci. Rep. 10, 1–15.
Bashiri, M., Geranmayeh, A.F., 2011. Tuning the parameters of an artificial neural network using central composite design and genetic algorithm. Sci. Iran. 18, 1600–1608.
Bauer-Marschallinger, B., Freeman, V., Cao, S., Paulik, C., Schaufler, S., Stachl, T., Modanesi, S., Massari, C., Ciabatta, L., Brocca, L., et al., 2018. Toward global soil moisture monitoring with Sentinel-1: harnessing assets and overcoming obstacles. IEEE Trans. Geosci. Remote Sens. 57, 520–539.
Belenguer-Plomer, M.A., Tanase, M.A., Fernandez-Carrillo, A., Chuvieco, E., 2018. Insights into burned areas detection from Sentinel-1 data and locally adaptive algorithms. In: Active and Passive Microwave Remote Sensing for Environmental Monitoring II, vol. 10788. International Society for Optics and Photonics, p. 107880G.
Belenguer-Plomer, M.A., Chuvieco, E., Tanase, M.A., 2019a. Evaluation of backscatter coefficient temporal indices for burned area mapping. In: Active and Passive Microwave Remote Sensing for Environmental Monitoring III, vol. 11154. International Society for Optics and Photonics, p. 111540D.
Belenguer-Plomer, M.A., Chuvieco, E., Tanase, M.A., 2019b. Temporal decorrelation of C-band backscatter coefficient in Mediterranean burned areas. Remote Sens. 11, 2661.
Belenguer-Plomer, M.A., Tanase, M.A., Fernandez-Carrillo, A., Chuvieco, E., 2019c. Burned area detection and mapping using Sentinel-1 backscatter coefficient and thermal anomalies. Remote Sens. Environ. 233, 111345.
Belenguer-Plomer, M.A., Chuvieco, E., Tanase, M.A., 2020. Optimum Sentinel-1 pixel spacing for burned area mapping. In: IGARSS 2020-2020 IEEE International Geoscience and Remote Sensing Symposium. IEEE, pp. 4858–4861.
Benedetti, A., Picchiani, M., Del Frate, F., 2018a. Sentinel-1 and sentinel-2 data fusion for urban change detection. In: IGARSS 2018-2018 IEEE International Geoscience and Remote Sensing Symposium. IEEE, pp. 1962–1965.
Benedetti, P., Ienco, D., Gaetano, R., Ose, K., Pensa, R.G., Dupuy, S., 2018b. M^3 fusion: a deep learning architecture for multiscale multimodal multitemporal satellite data fusion. IEEE J. Select. Top. Appl. Earth Observ. Remote Sens. 11, 4939–4949.
Bojinski, S., Verstraete, M., Peterson, T.C., Richter, C., Simmons, A., Zemp, M., 2014. The concept of essential climate variables in support of climate research, applications, and policy. Bull. Am. Meteorol. Soc. 95, 1431–1443.
Bourgeau-Chavez, L., Kasischke, E., Brunzell, S., Mudd, J., Tukman, M., 2002. Mapping fire scars in global boreal forests using imaging radar data. Int. J. Remote Sens. 23, 4211–4234.
Bouvet, A., Mermoz, S., Ballère, M., Koleck, T., Le Toan, T., 2018. Use of the SAR shadowing effect for deforestation detection with Sentinel-1 time series. Remote Sens. 10, 1250.
Bowman, D.M., Balch, J.K., Artaxo, P., Bond, W.J., Carlson, J.M., Cochrane, M.A., D'Antonio, C.M., DeFries, R.S., Doyle, J.C., Harrison, S.P., et al., 2009. Fire in the earth system. Science 324, 481–484.
Bowman, D., Williamson, G., Yebra, M., Lizundia-Loiola, J., Pettinari, M.L., Shah, S., Bradstock, R., Chuvieco, E., 2020. Wildfires: Australia Needs National Monitoring Agency.
Brown, A.R., Petropoulos, G.P., Ferentinos, K.P., 2018. Appraisal of the Sentinel-1 & 2 use in a large-scale wildfire assessment: a case study from Portugal's fires of 2017. Appl. Geogr. 100, 78–89.
Chan, S., Bindlish, R., O'Neill, P., Jackson, T., Njoku, E., Dunbar, S., Chaubell, J., Piepmeier, J., Yueh, S., Entekhabi, D., et al., 2018. Development and assessment of the SMAP enhanced passive soil moisture product. Remote Sens. Environ. 204, 931–941.
Chen, Q., Zeng, J., Cui, C., Li, Z., Chen, K.-S., Bai, X., Xu, J., 2018. Soil moisture retrieval from smap: a validation and error analysis study using ground-based observations over the little washita watershed. IEEE Trans. Geosci. Remote Sens. 56, 1394–1408.
Chuvieco, E., Aguado, I., Yebra, M., Nieto, H., Salas, J., Martín, M.P., Vilar, L., Martínez, J., Martín, S., Ibarra, P., et al., 2010. Development of a framework for fire risk assessment using remote sensing and geographic information system technologies. Ecol. Model. 221, 46–58.
Chuvieco, E., Lizundia-Loiola, J., Pettinari, M.L., Ramo, R., Padilla, M., Mouillot, F., Laurent, P., Storm, T., Heil, A., Plummer, S., 2018. Generation and analysis of a new global burned area product based on MODIS 250m reflectance bands and thermal anomalies. Earth Syst. Sci. Data Discuss 512, 1–24.
Chuvieco, E., Mouillot, F., van der Werf, G.R., San Miguel, J., Tanasse, M., Koutsias, N., García, M., Yebra, M., Padilla, M., Gitas, I., et al., 2019. Historical background and current developments for mapping burned area from satellite earth observation. Remote Sens. Environ. 225, 45–64.
Di Gregorio, A., 2005. Land Cover Classification System: Classification Concepts and User Manual. United Nations Food and Agriculture Organization.
Fernandez-Carrillo, A., Belenguer-Plomer, M., Chuvieco, E., Tanase, M., 2018. Effects of sample size on burned areas accuracy estimates in the Amazon Basin. In: Earth Resources and Environmental Remote Sensing/GIS Applications IX, vol. 10790. International Society for Optics and Photonics, p. 107901S.
Flannigan, M.D., Amiro, B.D., Logan, K.A., Stocks, B., Wotton, B., 2006. Forest fires and climate change in the 21 st century. Mitig. Adapt. Strateg. Glob. Chang. 11, 847–859.
Flannigan, M.D., Krawchuk, M.A., de Groot, W.J., Wotton, B.M., Gowman, L.M., 2009. Implications of changing climate for global wildland fire. Int. J. Wildland Fire 18, 483–507.
Franquesa, M., Vanderhoof, M.K., Libonati, R., Rodrigues, J.A., Setzer, A.W., Stavrakoudis, D., Gitas, I.Z., Roteta, E., Padilla, M., Chuvieco, E., 2020. Development of a standard database of reference sites for validating global burned area products. Earth Syst. Sci. Data Discuss. 1–20.
Fraser, R., Li, Z., Cihlar, J., 2000. Hotspot and NDVI differencing synergy (HANDS): a new technique for burned area mapping over boreal forest. Remote Sens. Environ. 74, 362–376.
Freeman, A., Durden, S.L., 1998. A three-component scattering model for polarimetric SAR data. IEEE Trans. Geosci. Remote Sens. 36, 963–973.
French, N.H., Bourgeau-Chavez, L.L., Wang, Y., Kasischke, E.S., 1999. Initial observations of Radarsat imagery at fire-disturbed sites in interior Alaska. Remote Sens. Environ. 68, 89–94.
Gao, B.-C., 1996. NDWI—A normalized difference water index for remote sensing of vegetation liquid water from space. Remote Sens. Environ. 58, 257–266.
García, M.L., Caselles, V., 1991. Mapping burns and natural reforestation using thematic mapper data. Geocarto Int. 6, 31–37.
Giglio, L., Loboda, T., Roy, D.P., Quayle, B., Justice, C.O., 2009. An active-fire based burned area mapping algorithm for the MODIS sensor. Remote Sens. Environ. 113, 408–420.
Giglio, L., Schroeder, W., Justice, C.O., 2016. The collection 6 MODIS active fire detection algorithm and fire products. Remote Sens. Environ. 178, 31–41.
Giglio, L., Boschetti, L., Roy, D.P., Humber, M.L., Justice, C.O., 2018. The collection 6 MODIS burned area mapping algorithm and product. Remote Sens. Environ. 217, 72–85.
Gimeno, M., San-Miguel-Ayanz, J., 2004. Evaluation of RADARSAT-1 data for identification of burnt areas in southern Europe. Remote Sens. Environ. 92, 370–375.
Hansen, M.C., Potapov, P.V., Moore, R., Hancher, M., Turubanova, S., Tyukavina, A., Thau, D., Stehman, S., Goetz, S., Loveland, T., et al., 2013. High-resolution global maps of 21st-century forest cover change. Science 342, 850–853.
Hoffmann, W.A., Schroeder, W., Jackson, R.B., 2002. Positive feedbacks of fire, climate, and vegetation and the conversion of tropical savanna. Geophys. Res. Lett. 29, 9–1.
Hollmann, R., Merchant, C.J., Saunders, R., Downy, C., Buchwitz, M., Cazenave, A., Chuvieco, E., Defourny, P., de Leeuw, G., Forsberg, R., et al., 2013. The ESA climate change initiative: satellite data records for essential climate variables. Bull. Am. Meteorol. Soc. 94, 1541–1552.
Hu, F., Xia, G.-S., Hu, J., Zhang, L., 2015. Transferring deep convolutional neural networks for the scene classification of high-resolution remote sensing imagery. Remote Sens. 7, 14680–14707.
Huang, S., Siegert, F., 2006. Backscatter change on fire scars in Siberian boreal forests in ENVISAT ASAR wide-swath images. IEEE Geosci. Remote Sens. Lett. 3, 154–158.
Imperatore, P., Azar, R., Calo, F., Stroppiana, D., Brivio, P.A., Lanari, R., Pepe, A., 2017. Effect of the vegetation fire on backscattering: an investigation based on Sentinel-1 observations. IEEE J. Select. Top. Appl. Earth Observ. Remote Sens. 10, 4478–4492.
Inglada, J., Christophe, E., 2009. The Orfeo Toolbox remote sensing image processing software. In: Geoscience and Remote Sensing Symposium, 2009 IEEE International, IGARSS 2009, vol. 4. IEEE (pp. IV–733).
Jin, Y., Roy, D.P., 2005. Fire-induced albedo change and its radiative forcing at the surface in northern Australia. Geophys. Res. Lett. 32.
Kasischke, E.S., Bourgeau-Chavez, L.L., French, N.H., 1994. Observations of variations in ERS-1 SAR image intensity associated with forest fires in Alaska. IEEE Trans. Geosci. Remote Sens. 32, 206–210.
Kellenberger, B., Marcos, D., Tuia, D., 2018. Detecting mammals in UAV images: best practices to address a substantially imbalanced dataset with deep learning. Remote Sens. Environ. 216, 139–153.
Key, C., Benson, N., 2004. Ground measure of severity, the composite burn index; and remote sensing of severity, the normalized burn ratio. In: G. T. R. RMRS-GTR-164 (Ed.), FIREMON: Fire Effects Monitoring and Inventory System chapter Landscape assessment (LA): Sampling and analysis methods. USDA Forest Service, Rocky Mountain Research Station, Ogden, pp. 1–51.
Kloster, S., Mahowald, N., Randerson, J., Lawrence, P., 2012. The impacts of climate, land use, and demography on fires during the 21st century simulated by CLM-CN. Biogeosciences 9, 509–525.
Knorr, W., Jiang, L., Arneth, A., 2016. Climate, CO 2 and human population impacts on global wildfire emissions. Biogeosciences 13, 267–282.
Krawchuk, M.A., Moritz, M.A., Parisien, M.-A., Van Dorn, J., Hayhoe, K., 2009. Global pyrogeography: the current and future distribution of wildfire. PLoS One 4, e5102.
Krizhevsky, A., Sutskever, I., Hinton, G.E., 2012. Imagenet classification with deep convolutional neural networks. In: Advances in Neural Information Processing Systems, pp. 1097–1105.

Kurum, M., 2015. C-band SAR backscatter evaluation of 2008 Gallipoli forest fire. IEEE Geosci. Remote Sens. Lett. 12, 1091–1095.
Kussul, N., Lavreniuk, M., Skakun, S., Shelestov, A., 2017. Deep learning classification of land cover and crop types using remote sensing data. IEEE Geosci. Remote Sens. Lett. 14, 778–782.
Langenfelds, R., Francey, R., Pak, B., Steele, L., Lloyd, J., Trudinger, C., Allison, C., 2002. Interannual growth rate variations of atmospheric CO2 and its δ13C, H2, CH4, and CO between 1992 and 1999 linked to biomass burning. Glob. Biogeochem. Cycles 16, 1048.
Langner, A., Miettinen, J., Siegert, F., 2007. Land cover change 2002–2005 in Borneo and the role of fire derived from MODIS imagery. Glob. Chang. Biol. 13, 2329–2340.
Lavorel, S., Flannigan, M.D., Lambin, E.F., Scholes, M.C., 2007. Vulnerability of land systems to fire: interactions among humans, climate, the atmosphere, and ecosystems. Mitig. Adapt. Strateg. Glob. Chang. 12, 33–53.
LeCun, Y., Bengio, Y., Hinton, G., 2015. Deep learning. Nature 521, 436.
Liu, Z., Ballantyne, A.P., Cooper, L.A., 2019. Biophysical feedback of global forest fires on surface temperature. Nat. Commun. 10, 1–9.
Lizundia-Loiola, J., Otón, G., Ramo, R., Chuvieco, E., 2020. A spatio-temporal active-fire clustering approach for global burned area mapping at 250 m from MODIS data. Remote Sens. Environ. 236, 111493.
Loboda, T., O'neal, K., Csiszar, I., 2007. Regionally adaptable dNBR-based algorithm for burned area mapping from MODIS data. Remote Sens. Environ. 109, 429–442.
Lu, B., He, Y., Tong, A., 2016. Evaluation of spectral indices for estimating burn severity in semiarid grasslands. Int. J. Wildland Fire 25, 147–157.
Ma, L., Liu, Y., Zhang, X., Ye, Y., Yin, G., Johnson, B.A., 2019. Deep learning in remote sensing applications: a meta-analysis and review. ISPRS J. Photogramm. Remote Sens. 152, 166–177.
Maggiori, E., Tarabalka, Y., Charpiat, G., Alliez, P., 2016. Convolutional neural networks for large-scale remote-sensing image classification. IEEE Trans. Geosci. Remote Sens. 55, 645–657.
Mandanici, E., Bitelli, G., 2016. Preliminary comparison of sentinel-2 and landsat 8 imagery for a combined use. Remote Sens. 8, 1014.
Melchiorre, A., Boschetti, L., 2018. Global analysis of burned area persistence time with MODIS data. Remote Sens. 10, 750.
Menges, C., Bartolo, R., Bell, D., Hill, G.E., 2004. The effect of savanna fires on SAR backscatter in northern Australia. Int. J. Remote Sens. 25, 4857–4871.
Mouillot, F., Schultz, M.G., Yue, C., Cadule, P., Tansey, K., Ciais, P., Chuvieco, E., 2014. Ten years of global burned area products from spaceborne remote sensing—a review: analysis of user needs and recommendations for future developments. Int. J. Appl. Earth Obs. Geoinf. 26, 64–79.
Nair, V., Hinton, G.E., 2010. Rectified linear units improve restricted boltzmann machines. In: Proceedings of the 27th International Conference on Machine Learning (ICML-10), pp. 807–814.
Olson, D.M., Dinerstein, E., Wikramanayake, E.D., Burgess, N.D., Powell, G.V., Underwood, E.C., D'amico, J.A., Itoua, I., Strand, H.E., Morrison, J.C., et al., 2001. Terrestrial Ecoregions of the world: a new map of life on earth: a new global map of terrestrial ecoregions provides an innovative tool for conserving biodiversity. BioScience 51, 933–938.
Ottinger, M., Clauss, K., Kuenzer, C., 2017. Large-scale assessment of coastal aquaculture ponds with sentinel-1 time series data. Remote Sens. 9, 440.
Padilla, M., Stehman, S.V., Chuvieco, E., 2014. Validation of the 2008 MODIS-MCD45 global burned area product using stratified random sampling. Remote Sens. Environ. 144, 187–196.
Padilla, M., Stehman, S.V., Ramo, R., Corti, D., Hantson, S., Oliva, P., Alonso-Canas, I., Bradley, A.V., Tansey, K., Mota, B., et al., 2015. Comparing the accuracies of remote sensing global burned area products using stratified random sampling and estimation. Remote Sens. Environ. 160, 114–121.
Padilla, M., Olofsson, P., Stehman, S.V., Tansey, K., Chuvieco, E., 2017. Stratification and sample allocation for reference burned area data. Remote Sens. Environ. 203, 240–255.
Padilla, M., Wheeler, J., Tansey, K., 2018. D4. 1.1 Product Validation Report (PVR). In: ESA CCI ECV Fire Disturbance. ESA Climate Change Initiative–Fire_cci.
Pausas, J.G., Paula, S., 2012. Fuel shapes the fire–climate relationship: evidence from Mediterranean ecosystems. Glob. Ecol. Biogeogr. 21, 1074–1082.
Pinto, M.M., Libonati, R., Trigo, R.M., Trigo, I.F., DaCamara, C.C., 2020. A deep learning approach for mapping and dating burned areas using temporal sequences of satellite images. ISPRS J. Photogramm. Remote Sens. 160, 260–274.
Plummer, S., Lecomte, P., Doherty, M., 2017. The ESA climate change initiative (CCI): a European contribution to the generation of the global climate observing system. Remote Sens. Environ. 203, 2–8.
Poulter, B., Cadule, P., Cheiney, A., Ciais, P., Hodson, E., Peylin, P., Plummer, S., Spessa, A., Saatchi, S., Yue, C., et al., 2015. Sensitivity of global terrestrial carbon cycle dynamics to variability in satellite-observed burned area. Glob. Biogeochem. Cycles 29, 207–222.
Quegan, S., Le Toan, T., Yu, J.J., Ribbes, F., Floury, N., 2000. Multitemporal ERS SAR analysis applied to forest mapping. IEEE Trans. Geosci. Remote Sens. 38, 741–753.
Ramo, R., Roteta, E., Bistinas, I., Van Wees, D., Bastarrika, A., Chuvieco, E., Van der Werf, G.R., 2021. African burned area and fire carbon emissions are strongly impacted by small fires undetected by coarse resolution satellite data. Proc. Natl. Acad. Sci. 118.
Roteta, E., Bastarrika, A., Padilla, M., Storm, T., Chuvieco, E., 2019. Development of a Sentinel-2 burned area algorithm: generation of a small fire database for sub-Saharan Africa. Remote Sens. Environ. 222, 1–17.
Rouse Jr., J., Haas, R., Schell, J., Deering, D., 1974. Monitoring vegetation systems in the Great Plains with ERTS. In: NASA. Goddard Space Flight Center 3d ERTS-1 Symp, vol. 1. NASA, pp. 309–317.
Roy, D.P., Boschetti, L., Justice, C.O., Ju, J., 2008. The collection 5 MODIS burned area product—global evaluation by comparison with the MODIS active fire product. Remote Sens. Environ. 112, 3690–3707.
Ruecker, G., Siegert, F., 2000. Burn scar mapping and fire damage assessment using ERS-2 SAR images in East Kalimantan, Indonesia. Int. Arch. Photogr. Remote Sens. 33, 1286–1293.
Saha, S., Bovolo, F., Bruzzone, L., 2019. Unsupervised deep change vector analysis for multiple-change detection in VHR images. IEEE Trans. Geosci. Remote Sens. 57, 3677–3693.
Scarpa, G., Gargiulo, M., Mazza, A., Gaetano, R., 2018. A CNN-based fusion method for feature extraction from sentinel data. Remote Sens. 10, 236.
Schmidhuber, J., 2015. Deep learning in neural networks: an overview. Neural Netw. 61, 85–117.
Schroeder, W., Oliva, P., Giglio, L., Csiszar, I.A., 2014. The new VIIRS 375 m active fire detection data product: algorithm description and initial assessment. Remote Sens. Environ. 143, 85–96.
Sharma, R., Hara, K., Tateishi, R., 2018. Developing Forest cover composites through a combination of Landsat-8 optical and Sentinel-1 SAR data for the visualization and extraction of forested areas. J. Imaging 4, 105.
Sitanggang, I., Yaakob, R., Mustapha, N., Ainuddin, A., 2013. Predictive models for hotspots occurrence using decision tree algorithms and logistic regression. J. Appl. Sci. 13, 252–261.
Strigl, D., Kofler, K., Podlipnig, S., 2010. Performance and scalability of GPU-based convolutional neural networks. In: 2010 18th Euromicro Conference on Parallel, Distributed and Network-based Processing. IEEE, pp. 317–324.
Stroppiana, D., Azar, R., Calò, F., Pepe, A., Imperatore, P., Boschetti, M., Silva, J., Brivio, P.A., Lanari, R., 2015. Integration of optical and SAR data for burned area mapping in Mediterranean regions. Remote Sens. 7, 1320–1345.
Tanase, M.A., Belenguer-Plomer, M.A., 2018. 03. D3 Intermediate validation results: SAR pre-processing and burned area detection, version 1.0. In: ESA CCI ECV Fire Disturbance. ESA Climate Change Initiative–Fire_cci.
Tanase, M.A., Santoro, M., Aponte, C., de la Riva, J., 2014. Polarimetric properties of burned forest areas at C-and L-band. IEEE J. Select. Top. Appl. Earth Observ. Remote Sens. 7, 267–276.
Tanase, M.A., Belenguer-Plomer, M.A., Roteta, E., Bastarrika, A., Wheeler, J., Fernández-Carrillo, Á., Tansey, K., Wiedemann, W., Navratil, P., Lohberger, S., et al., 2020. Burned area detection and mapping: Intercomparison of Sentinel-1 and Sentinel-2 based algorithms over tropical Africa. Remote Sens. 12, 334.
Tavares, P.A., Beltrão, N.E.S., Guimarães, U.S., Teodoro, A.C., 2019. Integration of sentinel-1 and sentinel-2 for classification and LULC mapping in the urban area of Belém, eastern Brazilian Amazon. Sensors 19, 1140.
Trigg, S., Flasse, S., 2001. An evaluation of different bi-spectral spaces for discriminating burned shrub-savannah. Int. J. Remote Sens. 22, 2641–2647.
Tucker, C.J., 1979. Red and photographic infrared linear combinations for monitoring vegetation. Remote Sens. Environ. 8, 127–150.
Turco, M., Jerez, S., Augusto, S., Tarín-Carrasco, P., Ratola, N., Jiménez-Guerrero, P., Trigo, R.M., 2019. Climate drivers of the 2017 devastating fires in Portugal. Sci. Rep. 9, 1–8.
Van Der Werf, G.R., Randerson, J.T., Giglio, L., Van Leeuwen, T.T., Chen, Y., Rogers, B. M., Mu, M., Van Marle, M.J., Morton, D.C., Collatz, G.J., et al., 2017. Global fire emissions estimates during 1997-2016. Earth Syst. Sci. Data 9, 697–720.
Van Tricht, K., Gobin, A., Gilliams, S., Piccard, I., 2018. Synergistic use of radar Sentinel-1 and optical Sentinel-2 imagery for crop mapping: a case study for Belgium. Remote Sens. 10, 1642.
Van Zyl, J.J., Arii, M., Kim, Y., 2011. Model-based decomposition of polarimetric SAR covariance matrices constrained for nonnegative eigenvalues. IEEE Trans. Geosci. Remote Sens. 49, 3452–3459.
Verhegghen, A., Eva, H., Ceccherini, G., Achard, F., Gond, V., Gourlet-Fleury, S., Cerutti, P.O., 2016. The potential of sentinel satellites for burnt area mapping and monitoring in the Congo Basin forests. Remote Sens. 8, 986.
Ward, D., Kloster, S., Mahowald, N., Rogers, B., Randerson, J., Hess, P., 2012. The changing radiative forcing of fires: global model estimates for past, present and future. Atmos. Chem. Phys. 12, 10857–10886.
Williams, A.P., Abatzoglou, J.T., 2016. Recent advances and remaining uncertainties in resolving past and future climate effects on global fire activity. Curr. Climat. Chang. Rep. 2, 1–14.
Wooster, M.J., Roberts, G., Perry, G., Kaufman, Y., 2005. Retrieval of biomass combustion rates and totals from fire radiative power observations: FRP derivation and calibration relationships between biomass consumption and fire radiative energy release. J. Geophys. Res.-Atmos. 110.
Xu, X., Li, W., Ran, Q., Du, Q., Gao, L., Zhang, B., 2017. Multisource remote sensing data classification based on convolutional neural network. IEEE Trans. Geosci. Remote Sens. 56, 937–949.
Zhang, C., Pan, X., Li, H., Gardiner, A., Sargent, I., Hare, J., Atkinson, P.M., 2018. A hybrid MLP-CNN classifier for very fine resolution remotely sensed image classification. ISPRS J. Photogramm. Remote Sens. 140, 133–144.
Zhang, C., Sargent, I., Pan, X., Li, H., Gardiner, A., Hare, J., Atkinson, P.M., 2019. Joint deep learning for land cover and land use classification. Remote Sens. Environ. 221, 173–187.

Zhong, Y., Fei, F., Liu, Y., Zhao, B., Jiao, H., Zhang, L., 2017. SatCNN: satellite image dataset classification using agile convolutional neural networks. Remote Sens. Lett. 8, 136–145.
Zhong, L., Hu, L., Zhou, H., 2019. Deep learning based multi-temporal crop classification. Remote Sens. Environ. 221, 430–443.
Zhu, X.X., Tuia, D., Mou, L., Xia, G.-S., Zhang, L., Xu, F., Fraundorfer, F., 2017. Deep learning in remote sensing: a comprehensive review and list of resources. IEEE Geosci. Remote Sens. Magaz. 5, 8–36.